Dry Reforming of Methane over Ni-Fe-Al Catalysts Prepared by Solution Combustion Synthesis

Manabayeva, Alua M.; Mäki-Arvela, Päivi; Vajglová, Zuzana; Martinéz-Klimov, Mark; Tirri, Teija; Baizhumanova, Tolkyn S.; Grigor'eva, Valentina P.; Zhumabek, Manapkhan; Aubakirov, Yermek A.; Simakova, Irina L.; Murzin, Dmitry Yu; Tungatarova, Svetlana A.

Published in:
Industrial and Engineering Chemistry Research

DOI:
10.1021/acs.iecr.3c00272

Published: 26/07/2023

Document Version
Final published version

Document License
CC BY

I&EC research
Industrial & Engineering Chemistry Research

pubs.acs.org/IECR

Article

Dry Reforming of Methane over Ni−Fe−Al Catalysts Prepared by Solution Combustion Synthesis

Alua M. Manabayeva,* Päivi Mäki-Arvela, Zuzana Vajglová, Mark Martinéz-Klimov, Teija Tirri, Tolkyn S. Baizhumanova, Valentina P. Grigor'eva, Manapkhan Zhumabek, Yermek A. Aubakirov, Irina L. Simakova, Dmitry Yu. Murzin,* and Svetlana A. Tungatarova

Cite This: *Ind. Eng. Chem. Res.* 2023, 62, 11439−11455

Read Online

ACCESS | Metrics & More | Article Recommendations | Supporting Information

ABSTRACT: Dry reforming of methane (DRM) is a promising method to utilize two greenhouse gases, such as CH_4 and CO_2, to produce synthesis gas. In the current work, both monometallic Ni and bimetallic Ni−Fe catalysts with different Fe/Ni molar ratios, synthesized by solution combustion synthesis (SCS) in DRM, were investigated using a feed ratio of $CH_4/CO_2/Ar$ of 1:1:1 at 600−900 °C. The catalysts were characterized by several physicochemical techniques such as X-ray diffraction (XRD), scanning electron microscopy energy-dispersive X-ray (SEM-EDX) spectroscopy, transmission electron microscopy (TEM), CHNS, N_2 physisorption, H_2-TPR, O_2-TPO, NH_3-TPD, and thermogravimetric analysis (TGA). One of the highest hydrogen yields of 81% was obtained at 93% conversion of CH_4 and 94% conversion of CO_2 for the bimetallic 15Ni−5Fe−30Al catalyst, which contained, according to XRD, $NiAl_2O_4$ spinel and metallic Ni phases. The spinel phase was decomposed during the reaction, while the Ni_3Fe alloy was formed. Catalysts with a higher Fe/Ni ratio exhibited lower conversion and contained an inactive $FeAl_2O_4$ spinel. Rather stable yields of CO and H_2 were obtained in an experiment with 20 h time-on-stream.

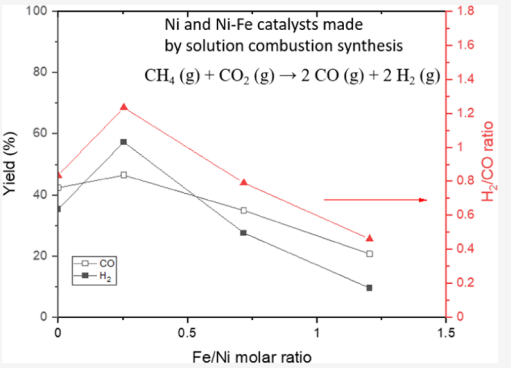

1. INTRODUCTION

Fossil fuels (such as oil, coal, and natural gas) are predominantly used nowadays, accounting for ca. 80% of all energy produced per year. The consumption of energy through the oxidation of fossil fuels inevitably leads to significant CO_2 emissions, accompanied by detrimental environmental problems such as global warming and climate change. Thus, much effort has been put into supplying renewable and sustainable energy from carbon-free resources (such as photovoltaic, solar thermal, wind, and tidal energy). While these alternative resources can provide heat and electricity, they are not capable of producing value-added products such as liquid/gaseous fuels and carbon-based organic chemicals.[1]

A significant role in recent decades has been played by technologies based on the use of waste, namely, anaerobic digestion of municipal solid waste in landfills, cattle manure, and urban wastewater, which allow the production of methane-rich gas, commonly referred to as raw biogas.[2]

Biogas is a gas mixture of products, consisting mainly of CH_4 and CO_2, although it has other impurities and gas products, the concentration of which can vary significantly depending on the feedstock and other factors, namely, the bacteria responsible for the anaerobic fermentation of these substrates. When properly processed, this gas has various energy applications, one of the most common being the production of heat and electricity through the direct combustion of raw biogas.[3,4] There is a growing interest in finding other uses for raw biogas, such as its use as a feedstock for the production of alternative, sustainable, and environmentally friendly biofuels, as well as valuable chemicals of industrial importance, such as synthesis gas (CO + H_2), through dry reforming. The latter has been widely proposed in the literature due to the direct utilization of both of the main raw biogas components (CH_4 and CO_2).[5] As a rule, the reaction is carried out using catalysts, which must be active, selective, stable, and cheap.

Besides dry reforming of methane (DRM)[6]

$$CH_4(g) + CO_2(g) \rightarrow 2CO(g) + 2H_2(g) \quad (1)$$

steam reforming of methane (SRM)[7] and partial oxidation of methane (POM)[8] can also occur.

$$CH_4(g) + H_2O(g) \rightarrow CO(g) + 3H_2(g) \quad (2)$$

$$CH_4(g) + 0.5O_2(g) \rightarrow CO(g) + 2H_2(g) \quad (3)$$

Received: January 30, 2023
Revised: June 27, 2023
Accepted: June 30, 2023
Published: July 18, 2023

The main disadvantage of DRM is a decrease in the catalytic activity with time-on-stream due to carbon formation. The carbon can be formed from methane decomposition and the Boudouard reaction, as demonstrated, respectively, below.

$$CH_4(g) \rightarrow C + 2H_2(g) \quad (4)$$

$$2CO(g) \rightarrow C + CO_2(g) \quad (5)$$

Noble metals, such as Rh, deposited on different supports have been used as catalysts in the dry reforming of methane, exhibiting high catalytic activity and stability with time-on-stream.[9] However, noble metal catalysts are more expensive than transition metals; subsequently, Ni-based catalysts were explored, resulting in the conclusion that they can be promising alternatives in dry methane reforming due to their comparably high activity. Although nickel-based catalysts are active in DRM, their activity can decrease as a result of metal sintering and coke formation. A reason for activity decline might also be the formation of a $NiAl_2O_4$ spinel phase at high temperatures, although this phase can be involved in the reaction pathway of carbon elimination in the DRM reaction.[10] To resolve this problem, a decrease in the Ni particle size and the application of suitable supports and promoters have been proposed. For example, nickel reacting with iron can form an alloy that improves the resistance to coke deposition.[11] In addition, Li et. al.[12] found that the use of Fe as a promoter increases the catalytic activity; subsequently, xNi−Fe−Al catalysts were found to be significantly more active than a Ni−Al catalyst without iron.[12] Furthermore, the special structure of the catalyst can enhance its stability and catalytic activity. According to the literature,[13] although the addition of iron improves stability, it can decrease the catalytic activity of iron-rich Ni−Fe catalysts.

Several Ni-based catalysts have been tested in DRM, with their textural properties, particle sizes, and process parameters summarized in Table 1.

A promising catalyst in DRM could be Ni/Al_2O_3 with highly dispersed small metal particles, which have stronger interactions with alumina (Table 1, entry 1). Accordingly, this catalyst was more active and stable, developing only a moderate amount of deposits, which were less graphitized.[14] In another work,[15] the addition of an alkaline-earth metal, such as Mg, to Ni/Al_2O_3 enhanced the nickel dispersion, improving the stability of the catalyst (Table 1, entry 2). The catalyst was stable in DRM for 200 h without visible deactivation. The presence of $NiAl_2O_4$, formed as a result of the strong interactions between Ni and alumina, is important in improving the catalyst stability during DRM. The following reaction mechanism for DRM over Ni−Fe−Mg(Al)O was proposed in ref.[16] CH_4 is adsorbed and decomposed on Ni active sites, whereas CO_2 undergoes activation at the metal−support interface and Fe sites (Table 1, entry 3). Thus, the formation of a Ni−Fe alloy can prevent coke deposition by inhibiting the cracking of CH_4. According to ref 17, the presence of 15 wt % La in the support is required to make it basic and, at the same time, improve the catalytic activity (Table 1, entry 4). It was additionally stated that NiO is highly dispersed in the $Ni/La_2O_3−Al_2O_3$ catalyst. When, however, increasing the La concentration to 20 wt %, the surface area, pore diameter, and pore volume decreased, making this catalyst inactive in DRM.

In solution combustion synthesis (SCS), which is a relatively unexplored method for catalyst preparation, typically, combustion of a solution containing metal precursors is carried out in the temperature range of 300−600 °C, using urea and glycine as

Table 1. Catalysts for the Dry Reforming of Methane[a]

entry	catalyst	reaction conditions	X_{CH_4}, %	X_{CO_2}, %	H_2/CO	S_{BET}, m^2/g	metal particle size, nm	TOS, h	ref
1	Ni/Al_2O_3	$CH_4/CO_2/N_2$ = 1:1:1, 750 °C, GHSV = 30,000 mL/h/g_{cat}	65	75	0.7	90	26	120	14
2	$Ni−Mg/Al_2O_3$	$CH_4/CO_2/N_2$ = 20:15:35 mL/min, 550−850 °C, GHSV = 10,000 mL/h/g_{cat}	90	99	1.2	153	14.5	200	15
3	Ni−Fe/Mg(Al)O	$CH_4/CO_2/N_2$ = 1:1:2, 500−800 °C, GHSV = 60,000 mL/g/h	92	98	0.9	138	8	25	16
4	$Ni−La/Al_2O_3$	$CH_4/CO_2/N_2$ = 1:1:0.3, 700 °C, GHSV = 42,000 mL/g/h	64	79	1	162	14	8	17

[a]X, conversion; TOS, time-on-stream; GHSV, gas hourly space velocity.

https://doi.org/10.1021/acs.iecr.3c00272
Ind. Eng. Chem. Res. 2023, 62, 11439−11455

oxidizing agents. In addition to catalysts, several other types of materials, such as semiconductors, bioceramics, luminescent nanospheres, and various types of nanosized oxides, can be synthesized.[18] It should be mentioned that the catalyst prepared via SCS can be active in DRM due to its small particle size, thereby increasing its catalytic activity.[19]

Catalysts derived by SCS are divided into two groups, such as bulk and supported. The first group of catalysts comprises powders or foam-like aggregates used in various catalytic reactions. The second group of catalysts is obtained from the deposition of active metals on a solid support at high temperature. In the first group of oxides, alloys and metals are formed. For instance, autothermal reforming of hydrocarbons is carried out over $LaFeO_3$ perovskites, which exhibit high activity and very good stability. It is important to mention that the temperature in a preheated furnace (300−600 °C) initiates a rapid high-temperature synthesis.[20,21] The first step of combustion is the evaporation of water in a few seconds and the formation of gels. The second step is the combustion of gels in air with flame, resulting in the formation of highly dispersed nickel particles with a size of 5 nm. Depending on the fuel used, nitrates and the fuel react in different ways. During explosion, heat, as well as CO_x and NO_x, is released. Therefore, the temperature of the flame is higher than the initiating temperature or preignition temperature (500 °C). It is important to notice that the solution cannot be burned at a furnace temperature below 300−600 °C. A higher temperature reduces the time of ignition and improves the crystallinity of the powders, i.e., catalysts.

It is reported that $NiAl_2O_4$ is formed at high temperatures during SCS.[22] The formation of $NiAl_2O_4$ was confirmed when different preignition temperatures, i.e., 500, 700, and 900 °C, were used in the SCS method.[22] The solution mixture was heated rapidly in the chamber. In addition, when the flaming point of the fuel was extended to the mixture, it was burned to form the powdered catalyst. According to ref,[22] X-ray diffraction (XRD) results showed that, together with $NiAl_2O_4$, NiO was also identified; however, Al_2O_3 was completely absent, in agreement with the current work.

The aim of this work is to study the effect of Fe on the catalytic activity and stability when using 15 wt % nickel nitrate together with varying amounts of iron and aluminum nitrates and 50 wt % urea as an oxidizing agent. Comprehensive characterization of the fresh and spent catalysts was performed using XRD, transmission electron microscopy (TEM), energy-dispersive X-ray (EDX) spectroscopy, CHNS, H_2-TPR, NH_3-TPD, O_2-TPO, and thermogravimetric analysis (TGA).

2. EXPERIMENTAL SECTION

2.1. Materials. For catalyst preparation, the chemical reagents shown in Table S1 were used. For laboratory experiments, gases such as methane, carbon dioxide, and argon were used, with their purity being 99%.

2.2. Catalyst Preparation via Solution Combustion. All necessary chemical reagents for the catalyst preparation were used without additional pretreatment. After weighing the required amounts of salts on an analytical balance, their mixture was placed in a thermostable beaker to which 15 mL of deionized water preheated to 80 °C was added. After the complete dissolution of all salts, the beaker with the solution was introduced in a preheated muffle furnace to 500 °C. The catalysts were synthesized under air. As a result, a powdered material was obtained by combustion of the solution. The beaker was cooled to room temperature under a fume hood. The catalysts were denoted based on the initial weight % of nickel(II) hexahydrate (x), iron(III) nonahydrate (y), and aluminum nitrate nonahydrate (z) as xNi−yFe−zAl, which comprised overall 50% of the weight, the remaining 50 wt % being urea in the solution.

2.3. Catalyst Characterization. The phase composition and structure of the synthesized catalysts were characterized by X-ray diffraction using a DRON-4-0.7 diffractometer (Russia) at the D.V. Sokolsky Institute of Fuel, Catalysis and Electrochemistry applying CoKα radiation and the powder method in a 2θ range of 5−100°.

The MicrotracBelcat II equipment was used to perform temperature-programmed reduction (TPR) measurements. Catalyst samples (ca. 100 mg) were pretreated at 200 °C for 2 h, followed by cooling to 50 °C and subsequent heating to 800 °C with a 10 °C/min ramp under 1.5 mL/min hydrogen and 28.5 mL/min argon (5 vol % H_2 and 95 vol % Ar), and the holding time at the target temperature was 20 min.

Temperature-programmed desorption (NH_3-TPD) of ammonia was also conducted with the MicrotracBelcat II equipment. The required amount (ca. 60−100 mg) of the catalyst sample was pretreated at 500 °C for 1 h. Then, the sample was cooled to 50 °C before being heated to 600 °C with a 10 °C/min ramp under 1.5 mL/min ammonia and 28.5 mL/min helium (5 vol % NH_3 and 95 vol % He). The holding time at the target temperature was 20 min.

Temperature-programmed oxidation (O_2-TPO) was carried out in the MicrotracBelcat II equipment connected to a mass spectrometer. The pretreatment of the catalyst sample (ca. 50 mg) was conducted at 300 °C for 2 h, followed by cooling to 50 °C and then heating to 865 °C with a 2 °C/min ramp under 1.5 mL/min oxygen and 28.5 mL/min argon (5 vol % O_2 and 95 vol % Ar). The holding time of the target temperature was 20 min.

CHNS analysis was performed using a Thermo Fisher Scientific Flash 2000 Organic Elemental Analyzer equipped with a TC detector. A furnace temperature of 950 °C was used. Four organic compounds, cystine, 2,5-bis(5-*tert*-butyl-benzoxazol-2-yl)thiophene, sulphanilimide, and methionine, were used as standards.

Scanning electron microscopy (SEM) measurements were performed using a Zeiss Leo Gemini 1530 scanning electron microscope equipped with a Thermo Scientific UltraDry silicon drift detector (SDD).

For thermogravimetric analysis (TGA) and differential thermal analysis (DTA), an SDT Q600 apparatus (TA Instruments) was used, operating under air with a flow rate of 100 mL/min and a heating rate of 10 °C/min.

A Jeol JEM-1400Plus with 120 kV acceleration voltage and 0.38 nm resolution and an OsisQuemesa 11 Mpix bottom-mounted digital camera were utilized to investigate the metal particle size and textural characteristics. The catalysts were reduced using the same reduction program as that before the catalytic experiments. Determination of the metal particle sizes was performed with ImageJ software.

A Micromeritics 3Flex-3500 was used to determine the textural properties. The catalyst samples (ca. 150 mg) were subjected to the first stage of pretreatment, where moisture from the catalyst was removed by degassing ex-situ under vacuum at 180 °C for 20 h. The sample was then pretreated in the physisorption equipment under vacuum at 180 °C for 5 h, followed by liquid nitrogen adsorption at −196 °C and various relative pressures. The Brunauer−Emmett−Teller (BET) and

https://doi.org/10.1021/acs.iecr.3c00272
Ind. Eng. Chem. Res. 2023, 62, 11439−11455

density functional theory (DFT) methods were used to calculate the specific surface area and the pore volume along with the pore size distribution.

2.4. Catalytic Experiments. A study of the catalytic activity of the synthesized catalysts was carried out in a catalytic flow unit (CFU-1). The activity of the catalysts was determined at various temperatures in the range of 600−900 °C with a step of 100 °C, followed by a measurement at 600 °C. The initial feed ratio was $CH_4/CO_2/Ar$ = 33%:33%:34% (vol), in line with previous studies.[23] The total flow of the gases was equal to 100 mL/min (GHSV 3000 h^{-1}). The samples were kept for 10 min at the analyzed temperature in the flow of reacting components, after which an online GC analysis of the reaction products was carried out. Then, the reaction temperature was elevated, and the analytical procedure was repeated in a similar manner.

0.3 g of the catalyst was placed in a quartz reactor with 20 mm diameter and 410 mm length. The catalyst with a grain size of 0.21−0.42 mm without any dilution was placed onto a layer of quartz wool, giving the solid layer a height of 5.0 mm. The volume of the catalytic bed was 1.6 mL, i.e., the bulk density was 0.19 g/mL. The impacts of internal mass transfer limitations are minor, if the Weisz−Prater criteria are met,[24,25] defined as the ratio of the effective (observed) reaction rate to the maximum effective rate of diffusion at the external surface

$$\varphi = \frac{r_{obs} r_p^2 RT}{p_{CH_4} D_{eff}} \leq 1 \tag{6}$$

where r_{obs} [mol/s/m^3] is the observed reaction rate, defined as $r_{obs} = r_{CH_4} \cdot \rho_{bulk}$ (in this case, the reaction rate of methane, r_{CH_4} [mol/s/kg], was higher than the reaction rate of carbon dioxide; ρ_{bulk} [kg/m^3] is the bulk density of the catalyst), r_p [m] is the radius of the catalyst particle, R [8.314 m^3·Pa/K/mol] is the gas constant, T [K] is the reaction temperature, p_{CH_4} [Pa] is the partial pressure of methane, and D_{eff} [m^2/s] is the effective diffusivity calculated according to the following equation[25]

$$D_{eff} = \frac{\varepsilon}{\tau} D_e \tag{7}$$

where the porosity/tortuosity factor ε/τ was taken as 0.1, and the diffusivity D_e was determined by the Bosanquet equation[25]

$$\frac{1}{D_e} = \frac{1}{D_{AB}} + \frac{1}{D_K} \tag{8}$$

where D_{AB} is the binary diffusivity in gases (methane and carbon dioxide) calculated by the Chapman−Enskog equation,[25] with a value of 1.56×10^{-4} m^2/s, and D_K is the Knudsen diffusivity[25] for methane in the 15Ni−5Fe−30Al catalyst with a pore radius of 3.6 nm (determined by the BJH desorption method from N_2 physisorption), which is equal to 2.86×10^{-6} m^2/s.

In the current case for the long-term experiment at 800 °C and 1 atm over the 15Ni−5Fe−30Al catalyst, the Weisz−Prater criterion, ϕ, was calculated to be 0.26, indicating that the internal mass transfer limitations can be neglected.

2.5. Analysis. Analysis of the initial mixture and the reaction products was carried out using a Chromos GC-1000 chromatograph with Chromos software and an Agilent Technologies 6890N chromatograph with TCD and FID detectors. The chromatograph was equipped with packed and capillary columns. The packed column was used for the analysis of the initial feed (CH_4, CO_2), products (H_2, CO), and C_2H_6, C_2H_4, C_3−C_4 hydrocarbons. The detector temperature was set at 200 °C, the inlet temperature was 280 °C, and the column temperature was 40 °C. The carrier gas flow (Ar) was 10 mL/min.

2.6. Definitions. The conversion of methane and carbon dioxide was calculated according to the following equations

$$X_{CH_4} = \frac{F_{CH_4,in} - F_{CH_4,out}}{F_{CH_4,in}} \times 100\% \tag{9}$$

$$X_{CO_2} = \frac{F_{CO_2,in} - F_{CO_2,out}}{F_{CO_2,in}} \times 100\% \tag{10}$$

in which $F_{i,in}$ and $F_{i,out}$ denote the molar flow of i in and out, respectively.

The turnover frequency was calculated according to the following equation[24]

$$TOF_{CH_4} = \frac{F_{CH_4,in} - F_{CH_4,out}}{n_{Ni(surface)}} \times 100\% \tag{11}$$

in which F_{CH_4} is the molar flow of methane, and n_{Ni}(surface) is the number of moles of exposed Ni calculated according to the equation

$$n_{Ni(surface)} = m_{cat} \frac{c_{Ni} D_{Ni}}{Mr_{Ni}} \tag{12}$$

In eq 12, m_{cat} is the mass of the catalyst, c_{Ni} is the concentration of Ni determined by EDX analysis, Mr_{Ni} is the molecular weight of nickel, and D_{Ni} is the Ni distribution. The dispersion of Ni was calculated using the formula described by Sholten et al.[26] assuming spherical shapes of Ni, yielding the equation given below

$$D_{Ni} = 101/d_{FeNi} \tag{13}$$

where d_{FeNi} is the metal particle size determined by TEM.

The yields of hydrogen and CO can be obtained as follows

$$Y_{H_2} = \frac{F_{H_2,out}}{2F_{CH_4,in}} \times 100\% \tag{14}$$

$$Y_{CO} = \frac{F_{CO_2,out}}{F_{CH_4,in} + F_{CO_2,in}} \times 100\% \tag{15}$$

The H_2/CO ratio is calculated as follows

$$H_2/CO = Y_{H_2}/Y_{CO} \tag{16}$$

The carbon balance (CB) was calculated as shown below[27]

$$CB = \frac{F_{CH_4,out} + F_{CO_2,out} + F_{CO,out}}{F_{CH_4,in} + F_{CO_2,in}} \times 100\% \tag{17}$$

3. RESULTS AND DISCUSSION

3.1. XRD Results. Both fresh and some spent catalysts were studied by XRD, and the results are shown in Table 2 and Figure 1. According to the XRD pattern, the 15Ni−35Al catalyst contains both $NiAl_2O_4$ and metallic Ni crystalline phases (Figure 1a). The relative intensities and positions of the reflexes are distinctive for the $NiAl_2O_4$ spinel structure [ASTM 71-964], and its lattice parameter was determined to be 8.076 Å, which is close to that reported in the literature.[28] The intensity of, especially, the nickel aluminate peak (311) at 45.2° was decreased in the spent catalyst,[29,30] and the intensity of the

https://doi.org/10.1021/acs.iecr.3c00272
Ind. Eng. Chem. Res. 2023, 62, 11439−11455

Table 2. Phases Present in the Fresh and Spent Catalysts[a]

catalyst	phases (fresh/nonreduced)	phases (spent, short test—10 min TOS at up to 900 °C)
15Ni−35Al	Ni, $NiAl_2O_4$	Ni, $NiAl_2O_4$
15Ni−5Fe−30Al	Ni, Ni_3Fe, $NiAl_2O_4$	Ni_3Fe, $Al_{2.667}O_4$, Al_3Ni_2
15Ni−15Fe−20Al	NiO, $FeAl_2O_4$	Ni_3Fe, Al_3Ni_2, $FeAl_2O_4$
15Ni−25Fe−10Al	NiO, Ni_3Fe, $FeAl_2O_4$	Ni_3Fe, Al_3Ni_2, $FeAl_2O_4$

[a]n.d., no data.

metallic nickel peak at 52° was higher than that of spinel.[30−32] On the other hand, the NiO phase (PDF# 00-047-1049) is definitely absent because characteristic reflexes at 2θ = 43.5, 50.7, and 74.5° are not found. Furthermore, γ-Al_2O_3 and θ-Al_2O_3 were not found in 15Ni−35Al, and their lattice parameters are also different from those of $NiAl_2O_4$, being 7.905[33] and 7.901 Å,[34] respectively.

According to XRD results, NiO is also absent in the fresh 15Ni−5Fe−30Al catalyst.[35] The cubic Ni^0 phase was also determined in the fresh 15Ni−5Fe−30Al at 52°.[36] This phase was, however, absent in the spent catalyst. On the other hand, in contrast to the current case, NiO and $NiAl_2O_4$ existed in the fresh catalysts, and after DRM, the NiO was reduced to metallic Ni.[35]

X-ray diffraction reflexes in the fresh 15Ni−5Fe−30Al catalyst at 52.1, 60.9, and 91.7° correspond to the Ni_3Fe alloy.[36,37] Furthermore, it was proposed in ref[37] that de-alloying occurs, leading to the formation of FeO.

$$CO_2 + Fe \rightarrow CO + FeO \quad (18)$$

When carbon is formed by the decomposition of methane

$$CH_4 \rightarrow 2H_2 + C \quad (19)$$

This carbon reacts further with FeO

$$C + FeO \rightarrow CO + Fe \quad (20)$$

helping thus to remove carbon from the catalyst surface and retain catalytic activity.

In the current case, under the conditions when only 10 min time-on-stream at each temperature was used, Ni_3Fe remained stable in 15Ni−5Fe−30Al. Furthermore, it was reported in ref 38 that $NiAl_2O_4$ is decomposed during DRM forming Ni^{2+}, which in turn is reduced to metallic nickel, observed as the reflex

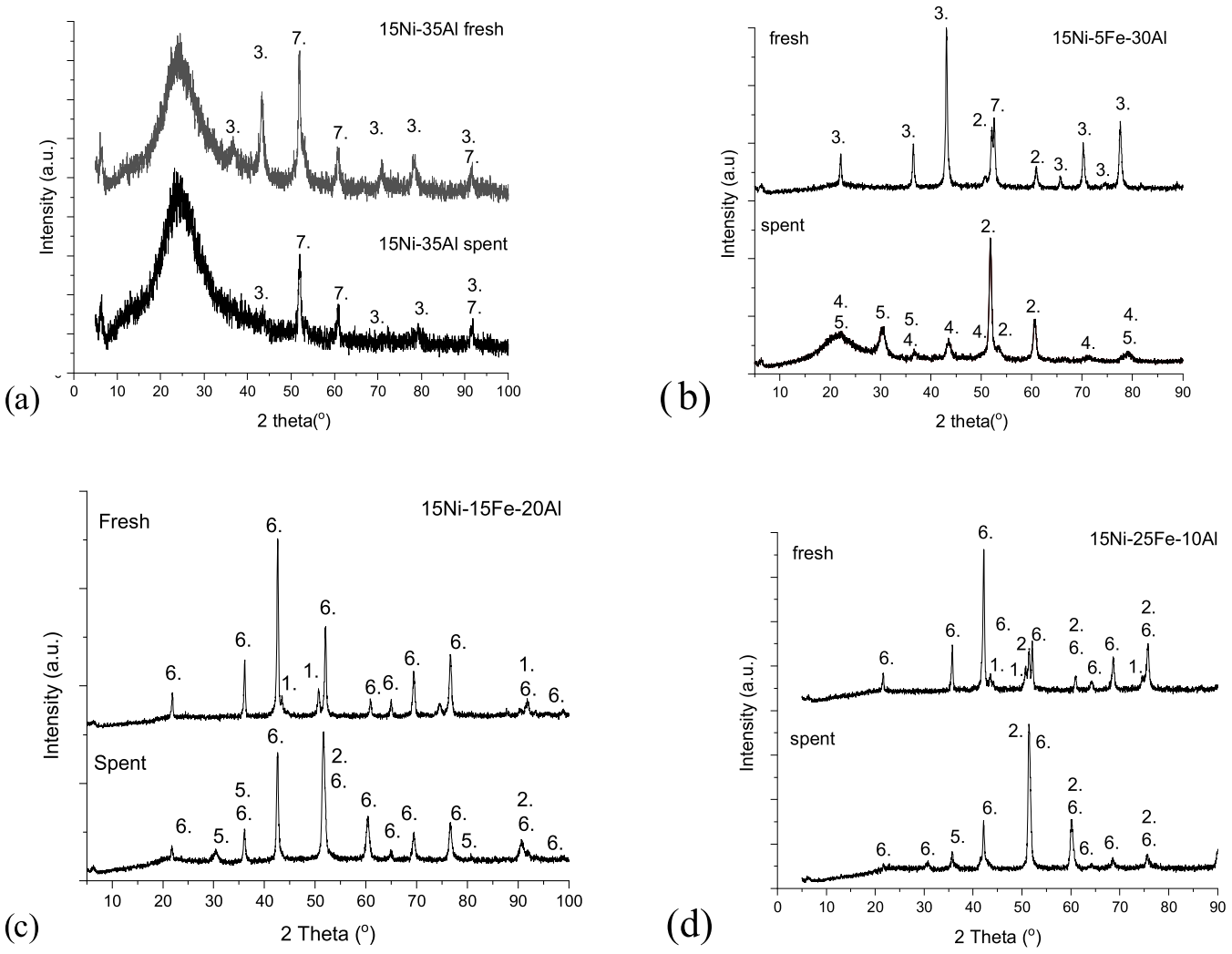

Figure 1. XRD patterns of the fresh and spent catalysts (short-term test—10 min TOS): (a) 15Ni−35Al, (b) 15Ni−5Fe−30Al, (c) 15Ni−15Fe−20Al, and (d) 15Ni−25Fe−10Al catalysts. Notations: 1, NiO [ASTM 47-1049]; 2, Ni_3Fe [ASTM 88-175]; 3, $NiAl_2O_4$ [ASTM 71-964]; 4, $Al_{2.667}O_4$ [ASTM 80-1385]; 5, Al_3Ni_2 [ASTM 14-468]; 6, $FeAl_2O_4$ [ASTM 86-2320]; and 7, Ni [ASTM-4-850].

https://doi.org/10.1021/acs.iecr.3c00272
Ind. Eng. Chem. Res. 2023, 62, 11439−11455

at 52 or 53°.[29] In addition, with metallic Ni in the spent 15Ni−5Fe−30Al, Al_3Ni_2 alloy and $Al_{2.667}O_4$ were also formed.[39−41] The latter phase was identified as the reflexes at 37 and 79°.[39] Furthermore, the Al−Ni alloy has reflexes at 31, 36, and 79°,[39] and only one reflex at 31° corresponds to Al_3Ni_2.[40,41] In contrast to other iron-containing catalysts, 15Ni−5Fe−30Al does not contain any $FeAl_2O_4$ in both the fresh and spent 15Ni−5Fe−30Al catalysts.

In the 15Ni−15Fe−20Al catalyst, the $FeAl_2O_4$ spinel phase and NiO were identified in the fresh sample, while in the spent sample, the reflex that corresponds to Ni_3Fe overlapped with those of the $FeAl_2O_4$ phase. NiO reflexes were present at 42 and 75° in ref.[42] The reflexes of 2θ = 36 (37), 42 (45), 52 (55), 60 (59), 65, and 76° were identified in both fresh and spent 15Ni−15Fe−20Al catalysts, corresponding to the $FeAl_2O_4$ spinel.[43,44] $FeAl_2O_4$ was also found in the 15Ni−25Fe−10Al catalyst, in reflexes of 30° (spent), 35° (fresh), 60.2° (59°), 65°, and 76°.[43,44] Furthermore, small reflexes of the Al_3Ni_2 alloy appeared to overlap with the reflex of the Ni_3Fe alloy. In the spent catalyst, a small reflex of the Al_3Ni_2 alloy was also identified. According to XRD data, $FeAl_2O_4$ was also found in the spent catalyst. In addition, XRD results of the long-term stability test showed the presence of Ni_3Fe and $NiAl_2O_4$, which are discussed in Section 3.7.2.

The Al_3Ni_2 alloy can be formed at high temperatures. The alloy could appear after DRM by the following reaction at 880, 940, and 1000 °C[45]

$$6NiO + 13Al \rightarrow 2Al_2O_3 + 3Al_3Ni_2$$

As can be seen, nickel oxide was reduced to Al_3Ni_2. The operating temperatures of the DRM reaction in the present work were in the range of 600−900 °C. In addition, taking into account the fact that NiO was present in the fresh 15Ni−15Fe−20Al and 15Ni−25Fe−10Al catalysts, the reduction of NiO can occur during DRM; thus, it is possible to explain the presence of the Al−Ni alloy in spent catalysts. The absence of NiO in fresh 15Ni−5Fe−30Al can be explained by its high dispersion in the catalyst.

3.2. TEM Analysis. The results of TEM showed well-dispersed metal particles (Figure 2). 15Ni−5Fe−30Al has the smallest Ni particle size among the studied catalysts (Figure 3), which can be a reason for its better catalytic performance.[12] In all spent catalysts, carbon nanotubes were observed,[46] indicating carbon formation on the catalyst surface, also confirmed by TGA and TPO. This result for bimetallic Ni−Fe−Al catalysts is in agreement with those reported in ref 47, wherein carbon filaments were observed in the Ni−Fe/Al_2O_3 catalyst. One reason for high coking over 15Ni−5Fe−30Al could be a high weight ratio of Ni/Fe of 4.1. Furthermore, metal particle sizes of all spent catalysts remain below 15 nm. The Ni particle sizes in carbon nanotubes for 15Ni−35Al and 15Ni−5Fe−30Al are approximately 24 and 27 nm, being 15 and 18 nm for 15Ni−15Fe−20Al and 15Ni−25Fe−10Al, respectively. It is important to mention that for Ni clusters larger than 9 nm, which is critical for coke formation, the carbon deposition is high.[48] 15Ni−25Fe−10Al has larger Ni particles (~26 nm), also in line with the XRD data, and the catalytically inactive $FeAl_2O_4$ remained partially stable in the spent catalyst. It was, however, observed that, for example, the reflex at 2θ = 42° decreased, indicating that $FeAl_2O_4$ can be reduced under DRM conditions (see TPR results). Generally, sintering of metal particles occurs during DRM, together with carbon nanotube formation; however, when nickel is embedded on the support and/or exhibits strong

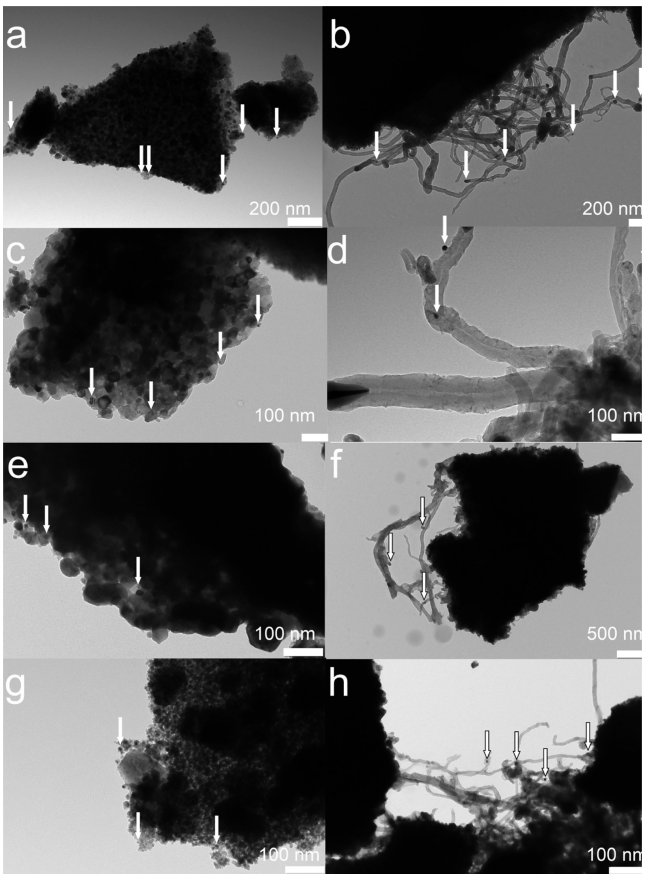

Figure 2. TEM images of (a) 15Ni−35Al fresh, (b) 15Ni−35Al spent, (c) 15Ni−5Fe−30Al fresh, (d) 15Ni−5Fe−30Al spent, (e) 15Ni−15Fe−20Al fresh, (f) 15Ni−15Fe−20Al spent, (g) 15Ni−25Fe−10Al fresh, and (h) 15Ni−25Fe−10Al spent catalysts.

interaction with the support, both sintering and carbon nanotube formation are suppressed.[46] For 15Ni−35Al and 15Ni−5Fe−30Al catalysts, strong metal−support interactions are visible in hydrogen TPR, showing the low reducibility of Ni (Figure 5), and thus, the Ni particle size remains nearly the same after DRM. For catalysts with a higher Fe loading, NiO in the fresh catalyst is reduced to the Ni_3Fe alloy during DRM. It was also reported in ref 12 that the particle size of the Ni_3Fe alloy phase in NiFeAl catalysts remained constant during DRM, while in the current work, this phase with a small particle size was formed during DRM.

In the current case, according to XRD results, Ni_3Fe was formed, and the metal particle size decreased during DRM over 15Ni−5Fe−30Al. As a comparison with the literature,[49] Ni particles were agglomerated in the 5Ni/La_2O_3 catalyst after 50 h of DRM at 650 °C, increasing the particle size to 17 nm, while for the Ni-impregnated mesoporous La_2O_3 spent catalyst, the Ni size was 5.5 nm, indicating that less sintering occurred. In the current case, no agglomeration of particles during DRM was observed, because the Ni particle size was decreased in the spent catalysts compared to the fresh catalysts. On the other hand, the addition of Fe to Ni-based catalysts can reduce the Ni nanoparticles, and also, the particle distribution becomes more narrow, which improves the catalytic activity in DRM.[47] It was mentioned that Ni tends to form an alloy with Fe; however, as reported in ref 50, the formation of the Ni−Fe alloy does not affect the metal particle size, and the metal particle size does not influence the catalytic properties. In addition, no sintering

https://doi.org/10.1021/acs.iecr.3c00272
Ind. Eng. Chem. Res. 2023, 62, 11439−11455

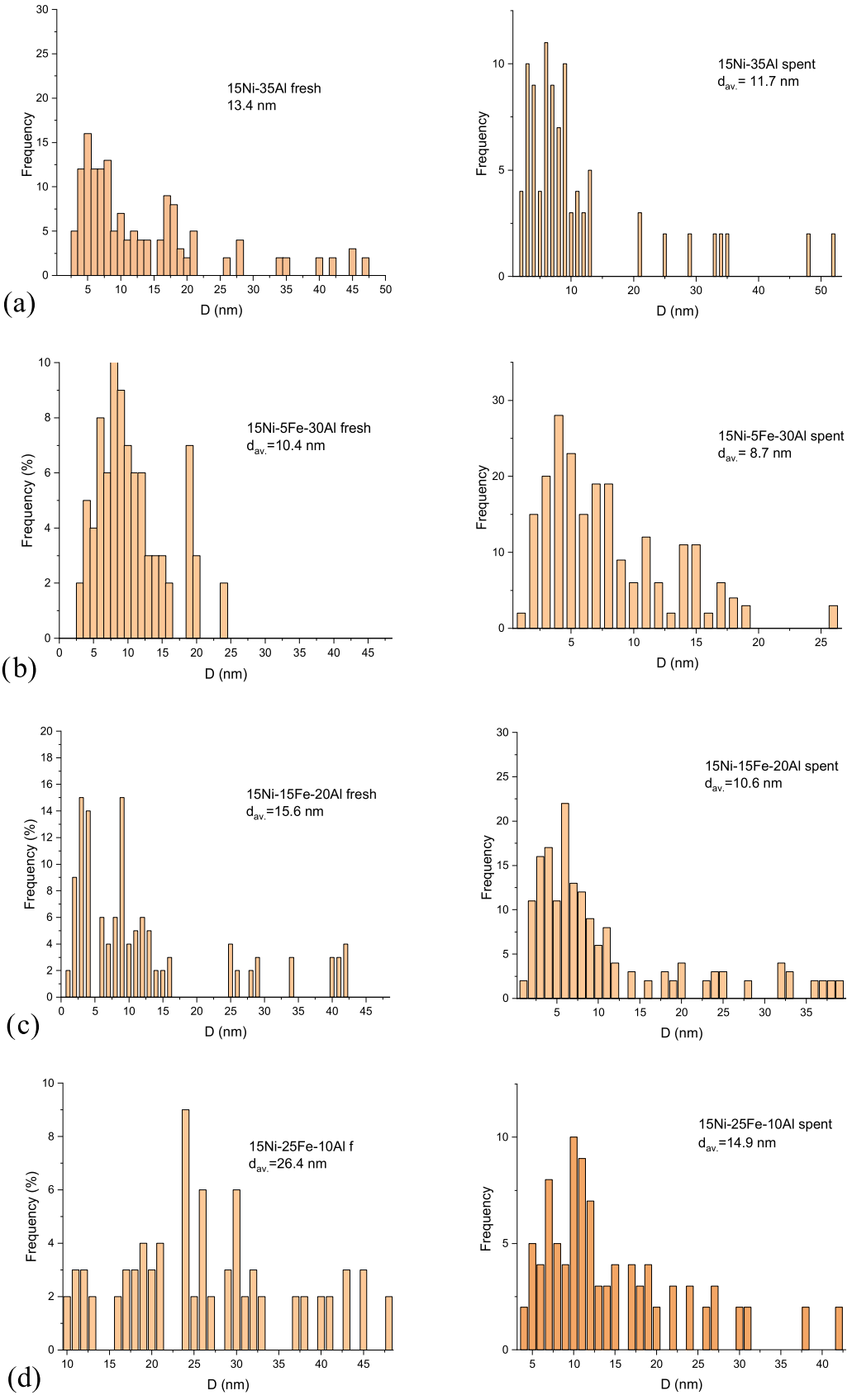

Figure 3. Histograms of the fresh and spent (a) 15Ni−35Al, (b) 15Ni−5Fe−30Al, (c) 15Ni−15Fe−20Al, and (d) 15Ni−25Fe−10Al catalysts. The spent catalysts were obtained from short-term DRM experiments using a GHSV of 3000 h^{-1}, 20 L/g/h, with CO_2/CH_4/Ar 33%:33%:34% and 10 min TOS at 600−700−800−900−600 °C.

https://doi.org/10.1021/acs.iecr.3c00272
Ind. Eng. Chem. Res. 2023, 62, 11439−11455

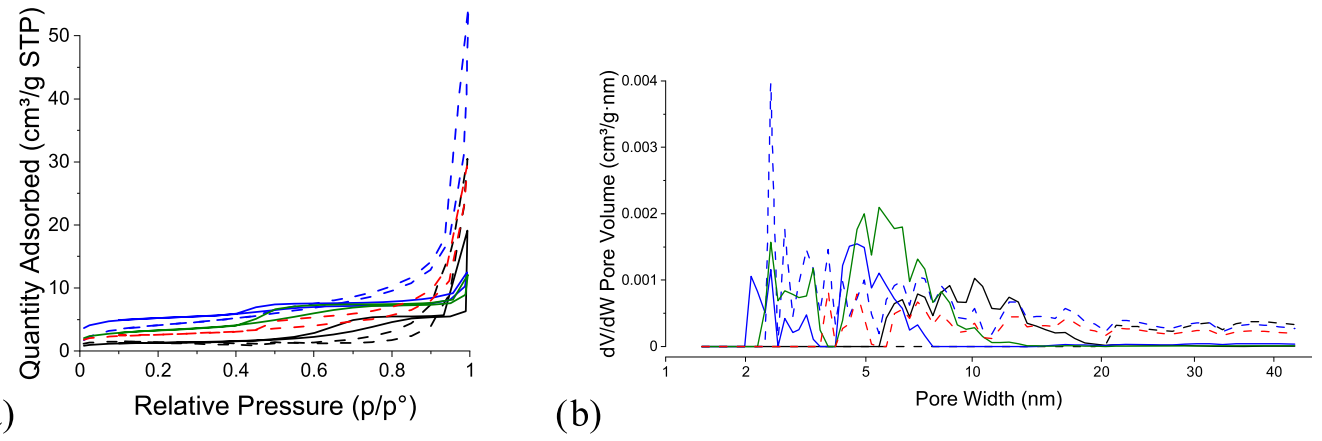

Figure 4. (a) Adsorption isotherms and (b) pore size distribution of the fresh and spent 15Ni−5Fe−30Al catalysts. Notations: 15Ni−35Al (red), 15Ni−5Fe−30Al (blue), 15Ni−15Fe−20Al (green), and 15Ni−25Fe−10Al (black). The solid line denotes the fresh catalyst and the dashed line denotes the spent catalyst. Spent catalysts were obtained from short-term DRM experiments using a GHSV of 3000 h^{-1}, 20 L/g/h, with CO_2/CH_4/Ar 33%:33%:34% and 10 min TOS at 600−700−800−900−600 °C.

Table 3. Textural Properties of Catalysts[a,b]

catalyst	S_{BET}, cm^3/g	V_{tot}, cm^3/g	V_μ cm^3/g	V_m, cm^3/g	V_μ/V_m	$d_{p,avg}$, nm
15Ni−35Al (f)	n.d.	n.d.	n.d.	n.d.	n.d.	9.2
15Ni−35Al (s)	8	0.014	0.004	0.011	0.33	16.3
15Ni−5Fe−30Al (f)	16	0.012	0.007	0.004	1.75	7.2
15Ni−5Fe−30Al (s)	14	0.021	0.003	0.018	0.19	8.0
15Ni−15Fe−20Al (f)	11	0.011	0.003	0.008	0.33	6.1
15Ni−15Fe−20Al (s)	9	0.019	0.001	0.018	0.06	12.2
15Ni−25Fe−10Al (f)	4	0.008	0.001	0.007	0.16	14.8
15Ni−25Fe−10Al (s)	<4	0.008	0.001	0.007	0.13	25.7

[a] V_{tot} denotes the total adsorbed volume; V_m and V_m denote the micro- and mesopore volumes, respectively; *f* and *s* denote fresh and spent catalysts, respectively; and $d_{p,avg}$ denotes the average pore diameter. [b] n.d., not determined.

occurred for $Sr_2Fe_xNi_{1-x}MoO_{6-\delta}$ double-layered perovskites after a 10 h stability test, and the metal particle size was in the range of values obtained before the reaction (ca. 31 nm).[51] Furthermore, it was concluded that carbon formation caused a slight decrease in the particle size.

3.3. SEM-EDX Analysis. SEM images of fresh and spent 15Ni−35Al and 15Ni−5Fe−30Al (Figure S2) show that the catalysts exhibit an irregular flake-like structure with dimensions in the range of 60−420 μm. The particles also contain surface cracks and microporosity. No major differences were observed in the shapes of the fresh and spent catalysts. For fresh 15Ni−5Fe−30Al, the catalyst surface appeared smooth; however, it was composed of small (1−3 μm) agglomerated particles (Figure S1e). Furthermore, in spent 15Ni−5Fe−30Al, carbon nanofibers were clearly visible. SEM-EDX analysis demonstrated that the weight ratio of Fe/Ni decreased from the fresh to the spent catalysts as follows: 4% for 15Ni−5Fe−30Al, 3% for 15Ni−15Fe−20Al, and 2.5% for 15Ni−25Fe−10Al (Table S2). The oxygen content decreased by 60% for 15Ni−5Fe−30Al when its amount in the fresh catalyst was compared with the spent one, while the decrease in the oxygen content was the second largest for spent 15Ni−15Fe−20Al and the lowest for spent 15Ni−35Al. This can be explained by phase changes, i.e., the amount of Ni aluminate decreased substantially in 15Ni−5Fe−30Al. In addition, the Al/Ni weight ratio increased from fresh to spent catalysts by 20% for 15Ni−5Fe−30Al and 15Ni−25Fe−10Al, while this ratio increased by only 12.6% for 15Ni−15Fe−20Al. The same is valid for the Al/Fe weight ratio in which the corresponding increase is 27% for 15Ni−5Fe−30Al, 14% for 15Ni−15Fe−20Al, and 24% for 15Ni−25Fe−10Al.

When the Fe/Ni molar ratio is equal to or above 0.7, the intensity of diffraction reflexes decreases, indicating that the crystallinity was lower for a higher Fe loading.[12]

3.4. Nitrogen Physisorption. The results of textural property analysis are presented in Figure 4 and Table 3. All isotherms exhibited type IV hysteresis, which indicates the presence of mesopores. For the 15Ni−5Fe−30Al fresh catalyst, the BET surface area was 16 m^2/g for the synthesized catalyst and 14 m^2/g for the spent catalyst. The surface areas of the fresh 15Ni−25Fe−10Al catalysts were 4 m^2/g, being slightly below 4 m^2/g in the spent catalyst. It was also possible to correlate the amount of carbon in the spent catalyst with the increase in the adsorbed volume in nitrogen physisorption because the highest amount of coke was observed in 15Ni−5Fe−30Al, which exhibited the highest pore volume among spent catalysts, followed by 15Ni−35Al. The latter displayed the second highest carbon content based on CHNS analysis.

3.5. Hydrogen TPR. The hydrogen consumption (reducibility) of the Ni−Al and Ni−Fe−Al catalysts was studied by temperature-programmed reduction with H_2 (Figure 5 and Table 4). The maximum peak was observed at 470 °C, which was related to different levels of NiO interactions with the Al_2O_3 support in accordance with previous studies.[52] The reduction profile of 15Ni−5Fe−30Al revealed a single peak at about 467 °C along with a small shoulder at 403 °C. For $NiAl_2O_4$, also present on the fresh 15Ni−5Fe−30Al catalyst according to XRD, it has been reported that reduction starts already at 742

https://doi.org/10.1021/acs.iecr.3c00272
Ind. Eng. Chem. Res. 2023, 62, 11439−11455

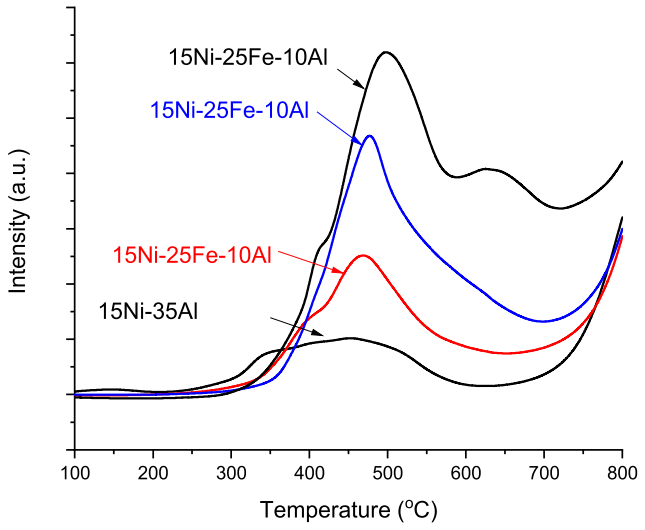

Figure 5. Temperature-programmed reduction of Ni−Fe catalysts.

°C,[52,53] which would explain the hydrogen consumption at a high temperature. The TPR results confirm the presence of small Ni particles with uniform size, eliminating the possible formation of larger agglomerates on the catalyst, which would result in reduction peaks at lower temperatures.[52] A second reduction peak appeared for catalysts with a higher amount of Fe.[54]

As can be seen in Figure 5, the higher the iron loading, the higher the amount of hydrogen consumed for 15Ni−25Fe−10Al above 600 °C, which could be related to the reduction of the hercynite phase, $FeAl_2O_4$, reported to occur at 665 °C.[55]

3.6. Acidity of Different Catalysts. The acidity of different catalysts determined by ammonia TPD is shown in Table 5 and Figure 6, illustrating that it increased with increasing aluminum content. The peak for the maximum adsorption of ammonia also shifted toward higher temperatures with increasing iron content, indicating a higher amount of strong acid sites.

As can be seen from the CHNS results (Table 6), the higher the amount of iron, the lower the amount of carbon formed during the reaction. It was reported in the literature[54] that iron-promoted Ni-based catalysts are more coke resistant. On the other hand, the amount of carbon can reflect more active centers during DRM. Here, the spent catalyst 15Ni−5Fe−30Al has the highest amount of carbon, which correlated with higher catalytic activity in DRM among other catalysts. The calculated molar ratios of H/C for 15Ni−5Fe−30Al and 15Ni−25Fe−10Al were 0.08 and 0.19, respectively, also showing that the type of coke was different. In particular, the former catalyst contained more graphitic coke in comparison to the latter one.

The TGA results (Figure 7, Table 6) demonstrated that more coke was obtained with 15Ni−15Fe−20Al than with 15Ni−25Fe−10Al, which can be correlated with the lower acidity of the latter catalyst.

Table 5. Results of Ammonia TPD

catalyst	$T_{max,1}$, °C	$T_{max,2}$, °C	relative area of NH_3 desorbed normalized by catalyst mass
15Ni−35Al	129	621	1.0
15Ni−5Fe−30Al	129	621	0.82
15Ni−15Fe−20Al	198	621	0.55
15Ni−25Fe−10Al	173	621	0.33

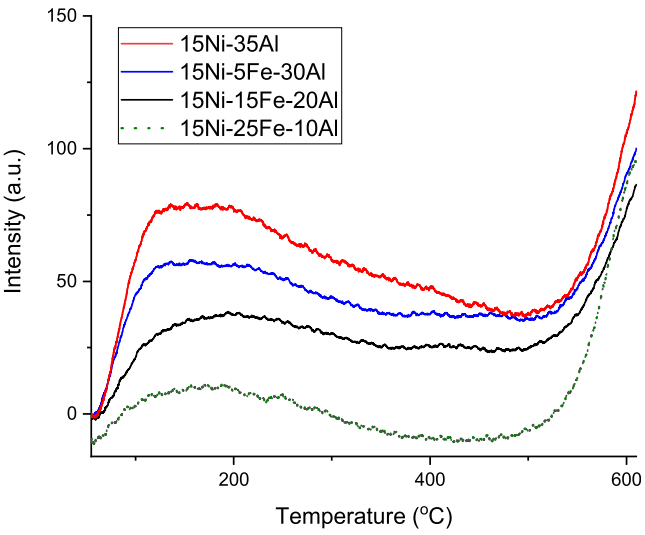

Figure 6. Ammonia TPD of the catalysts.

The results of TPO show that the temperature for the largest peak from 15Ni−25Fe−10Al was 671 °C, while the maximum carbon release was observed at 709 °C for 15Ni−15Fe−20Al (Figure 8). It was stated in ref[56] that carbon released above 650 °C corresponds to the pyrolytic type of inert coke. For 15Ni−5Fe−30Al, the intensity was the highest due to high heat development, because this catalyst contained a very high amount of coke (44 wt %), as confirmed by CHNS analysis. According to TPO results, the relative area for carbon dioxide release for 15Ni−15Fe−20Al was 0.41- and 0.47-fold that of 15Ni−25Fe−10Al.

According to the coke analysis, the highest amount of carbon was obtained for 15Ni−5Fe−30Al in accordance with TGA results. On the other hand, it was reported that the highest weight loss of 12% was observed in Ni/Al_2O_3 in the temperature range of 650−800 °C in DRM, while for $Ni-Fe/Al_2O_3$, it was only 6%.[25] The catalyst contained 3.95 wt % Ni and 5.14 wt % Fe, while in the current case, the Ni and Fe contents were 35 and 9 wt %, respectively, indicating that the excess of Ni was much larger.[27] Analogously, lower carbon formation was observed in the bimetallic Fe−Ni−Al catalyst in comparison to the monometallic Ni/Al_2O_3 catalyst in DRM at 700 °C,[12] when

Table 4. Results of the Temperature-Programmed Reduction[a]

catalyst	$T_{max,1}$, °C	$T_{max,2}$, °C	$T_{max,3}$, °C	$T_{max,4}$, °C	relative area of consumed H_2
15Ni−35Al	454	800	n.a.	n.d.	0.35
15Ni−5Fe−30Al	403	467	800	n.d.	0.57
15Ni−15Fe−20Al	477	800	n.d.	n.d.	0.79
15Ni−25Fe−10Al	417	500	630	800	1

[a]n.d., not detected.

https://doi.org/10.1021/acs.iecr.3c00272
Ind. Eng. Chem. Res. 2023, 62, 11439−11455

Table 6. Results of TGA, TPO, and CHNS Analyses of Spent Catalysts, which were Obtained from Short-Term DRM Experiments using a GHSV of 3000 h^{-1}, 20 L/g/h, with CO_2/CH_4/Ar 33%:33%:34% and 10 min TOS at 600−700−800−900−600 °C

catalyst	weight loss by TGA, %[a]	TPO relative area	carbon, wt %	nitrogen, wt %	hydrogen, wt %
15Ni−35Al	14	n.d.	19.3	0.04	0.2
15Ni−5Fe−30Al	40	1.0	44.2	0.18	0.3
15Ni−15Fe−20Al	n.d.	0.41	16.5	0.05	0.2
15Ni−25Fe−10Al	n.d.	0.47	10.7	0.38	0.2

[a]Between 100 and 800 °C; n.a., not available; n.d. not determined.

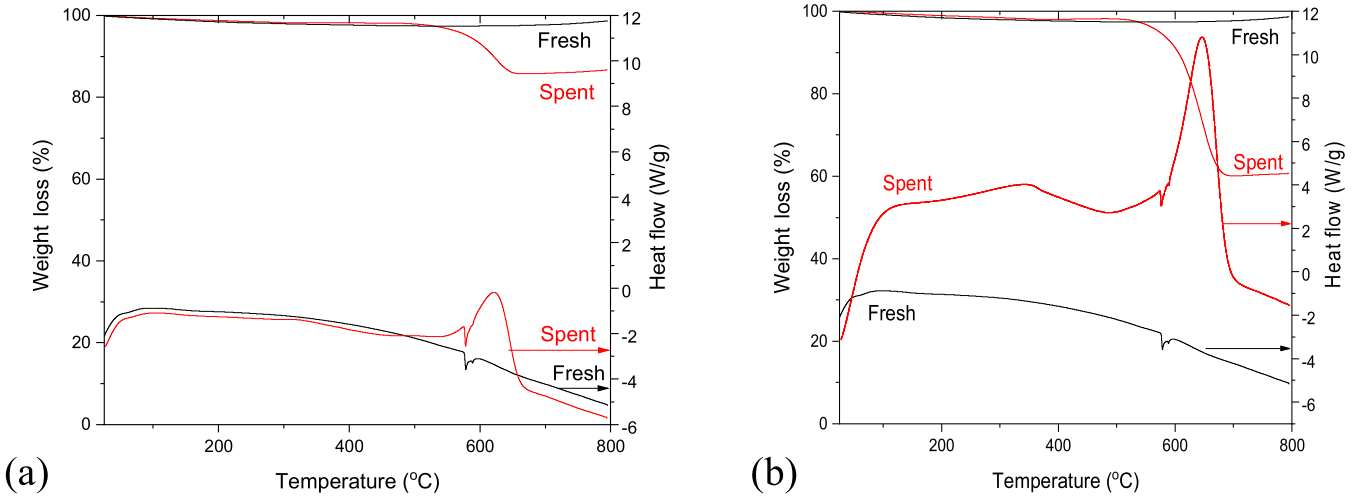

Figure 7. TGA results from fresh and spent (a) 15Ni−35Al and (b) 15Ni−5Fe−30Al catalysts.

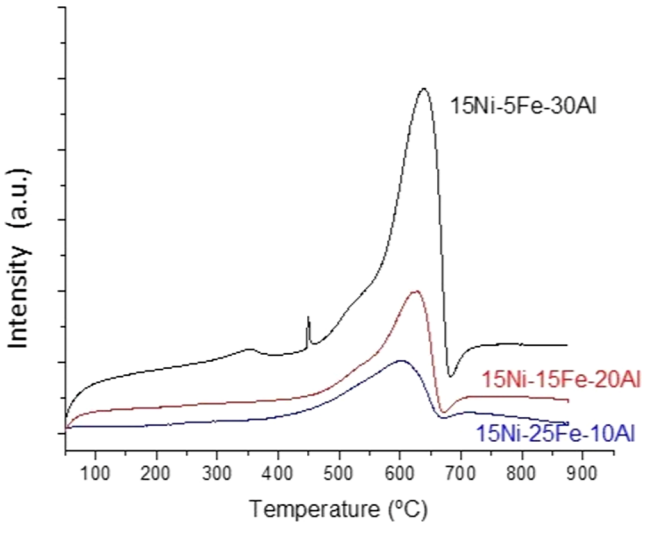

Figure 8. Results of TPO.

the molar ratio of Fe/Ni was 0.5. In the current case, the molar ratio of Fe/Ni for 15Ni−5Fe−30Al is only 0.27, which can explain the high coke formation.

3.7. Catalytic Results. *3.7.1. Effect of Iron Loading on the Activity, Selectivity, and Stability.* The effect of iron loading was investigated at 700 and 800 °C in the current work (Figure 9). As can be seen in Figure 9a, the conversions of CH_4 and CO_2 for the 15Ni−35Al catalyst are lower than for those for the catalyst with the lowest Fe/Ni ratio, i.e., 15Ni−5Fe−30Al. This result is different from the results of Li et al.,[12] in which both methane and CO_2 conversion increased when the Fe/Ni molar ratio reached a value of 0.7. When the Fe/Ni molar ratio was 0.9, lower CO_2 and CH_4 conversions were obtained. This difference in activity cannot be explained by the metal particle sizes, which were the same for all catalysts, ca. 7 nm;[12] however, in their case, the hydrogen uptake decreased with an increasing Fe/Ni molar ratio. It was also concluded that bimetallic Ni−Fe−Al catalysts were superior in comparison to their monometallic Ni−Al counterparts, and especially, the Ni−Fe alloy enhances the methane cracking determining activity in DRM.[12] When a large iron loading is used in Ni−Fe−Al catalysts, Fe species are only partially present in the alloy, which is active in DRM. Furthermore, it was observed that surface enrichment of Fe occurred during catalyst reduction.[12]

A higher conversion at 700 °C was observed over the catalyst with the lowest iron content, i.e., 15Ni−5Fe−30Al (Figure 9a). The yields of H_2 and CO for this catalyst are also higher than those for 15Ni−15Fe−20Al and 15Ni−25Fe−10Al catalysts, while the lowest yields were obtained over 15Ni−25Fe−10Al (Figure 9b). The catalyst with the lowest iron content, 15Ni−5Fe−30Al, was active due to the $NiAl_2O_4$ spinel, which, however, was not present after DRM. On the other hand, XRD exhibited reflexes of $Al_{2.667}O_4$ and Al_3Ni_2. It was reported in the literature[54] that the presence of Ni-aluminate and lower amounts of metallic nickel led to the suppression of coking. Further transformation of this phase, as observed for 15Ni−5Fe−30Al, would result in a more prominent coking in line with TPO and CHNS data for this catalyst.

In the current case, CO_2 conversion was always slightly higher than the conversion of methane (Figure 9a,c), analogous to the results obtained in the work of Li et al.[12] From the TEM analysis, the metal particle size of 15Ni−35Al was larger in comparison with that of 15Ni−5Fe−30Al, which could explain the lower activity of the former catalyst. It is confirmed in ref 57 that a high

https://doi.org/10.1021/acs.iecr.3c00272
Ind. Eng. Chem. Res. 2023, 62, 11439−11455

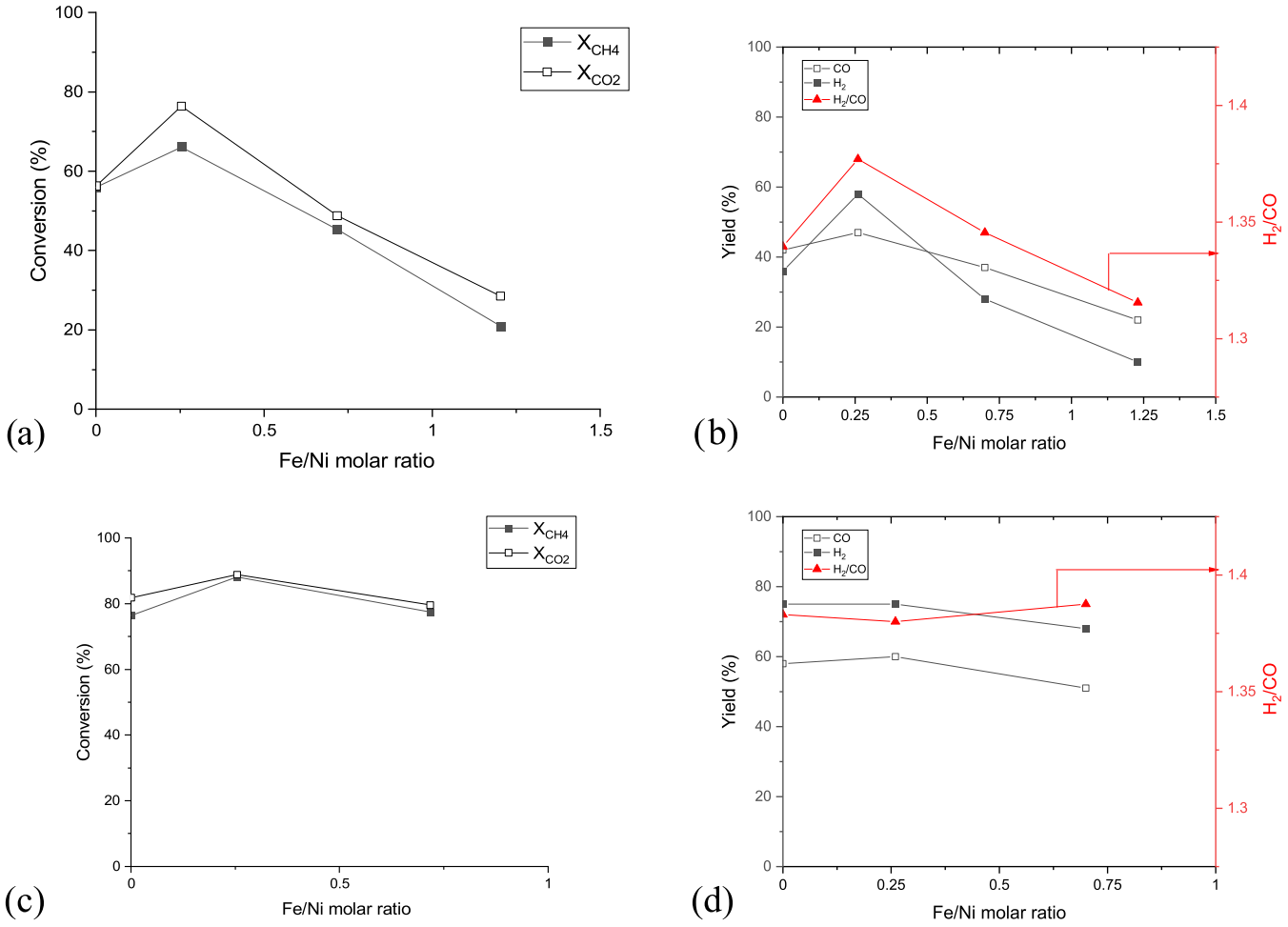

Figure 9. Influence of the Fe/Ni molar ratio on the conversion of CO_2 and CH_4 at (a) 700 °C and (c) 800 °C; the yield of H_2 and CO at (b) 700 °C and (d) 800 °C.

Table 7. Catalytic Results from DRM over Different Catalysts[a]

entry	catalyst	metal particle size (nm)	conditions	X_{CH_4}, %	X_{CO_2}, %	H_2/CO	TOF, s^{-1}	reference
			Temperature 600 °C					
1	15Ni−35Al	13	GHSV = 3000 h^{-1}, 20 L/g/h, CO_2/CH_4/Ar 33 vol %:33 vol %:34 vol %	27	28	0.5	0.03	this work
2	15Ni−5Fe−30Al	10		39	46	0.9	0.05	this work
3	15Ni−15Fe−20Al	16		21	25	0.7	0.04	this work
4	15Ni−25Fe−10Al	26		n.a.	n.a.	n.a.	n.a.	this work
5	5 wt % Ni/silica	3.3	GHSV = 600 h^{-1}, 60 L/g/h, CO_2/CH_4/He 1:1:1	54	54	0.98	2.46	64
6	5.8 wt % Ni-HMS	3.9	GHSV = 240 h^{-1}	<20%	n.a.	n.a.	5.67	63
			Temperature 700 °C					
7	4 wt % Ni−5.1 wt % Fe/Al_2O_3	n.a.	GHSV = 3200 h^{-1}, 8.4 L/g/h, CO_2/CH_4 = 1:1	92	n.a.	n.a.	n.a.	27
8	Ni−Al	n.a.	GHSV = 24 L/g/h, CH_4/CO_2He = 10 vol %:10 vol %:80 vol %	52	n.a.	n.a.	n.a.	27
9	0.3-FeNiAl	7		52	61	n.a.	n.a.	12
10	0.5-FeNiAl	7		57	63	n.a.	n.a.	12
11	0.7-FeNiAl	7		60	67	n.a.	n.a.	12
12	0.9-FeNiAl	9		62	69	n.a.	n.a.	12

[a]n.a., not available.

metal dispersion can improve the catalytic activity. On the other hand, the Ni-CeO_2 nanorod catalyst with the largest Ni particle size exhibited the highest activity.[58] Furthermore, coke formation was low for well-dispersed Ni-based catalysts.[59] However, in the current case, the most active bimetallic catalyst, 15Ni−5Fe−30Al (Table 7, entry 2), among other Ni−Fe catalysts, produced a substantial amount of carbon.

The effect of temperature was investigated by increasing the temperature after 10 min time-on-stream from 600 to 900 °C with a 100 °C step. For the best bimetallic catalyst with the smallest metal particle size among other Ni−Fe catalysts, i.e., 15Ni−5Fe−30Al, the stability test was also performed by restoring the temperature from 900 to 600 °C (Figure 10c,d). The results demonstrated that at 600 °C, the highest methane

https://doi.org/10.1021/acs.iecr.3c00272
Ind. Eng. Chem. Res. 2023, 62, 11439−11455

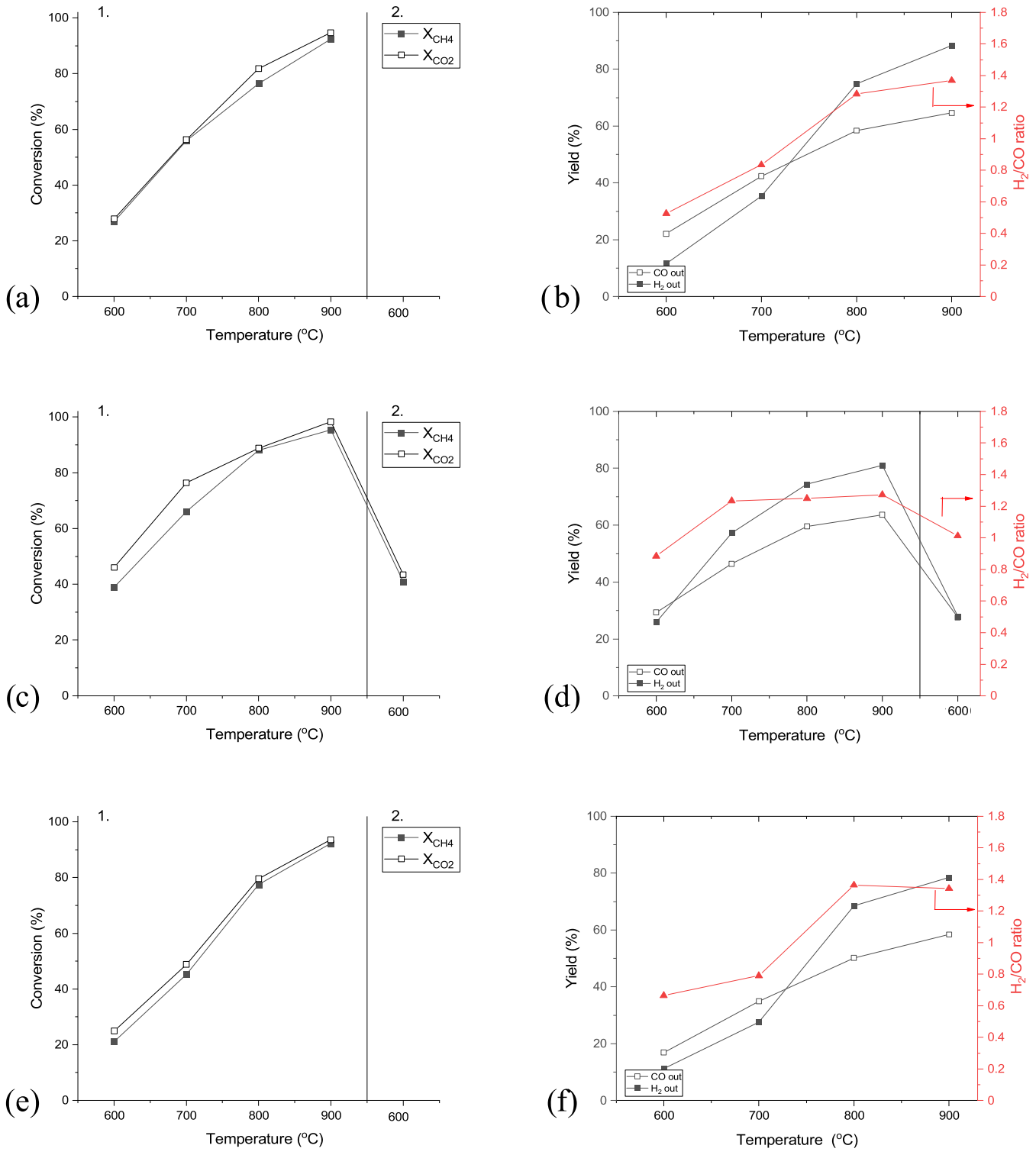

Figure 10. Effect of temperature on the (a, c, e) conversion of CH_4 and CO_2 and (b, d, f) yields of CO and H_2 and the H_2/CO ratio in dry methane reforming for (a, b) 15Ni−35Al, (c, d) 15Ni−5Fe−30Al, and (e, f) 15Ni−15Fe−20Al catalysts. GHSV = 3000 h^{-1}, 300 mg catalyst, 100 mL/min.

conversion was obtained over 15Ni−5Fe−30Al and the second highest over the 15Ni−35Al catalyst (Table 7), while catalysts with higher iron loadings were less efficient due to a large nickel particle size.[60] The 15Ni−5Fe−30Al catalyst also displayed relatively high stability, yielding nearly the same methane conversion after being tested at 700−900 °C and thereafter restoring to 600 °C despite high coking (Figure 10c,d, Table 7). The conversion of CH_4 and CO_2 for the 15Ni−15Fe−20Al catalyst increased respectively in the range of 21−92% and 25−94% at 600−900 °C (Figure 10e).

H_2 yields of 57, 35, 28, and 10% at 700 °C were obtained in the order of 15Ni−5Fe−30Al > 15Ni−35Al > 15Ni−15Fe−20Al > 15Ni−25Fe−10Al, respectively. The corresponding hydrogen yields over different catalysts at 800 °C were 75% (15Ni−35Al), 74% (15Ni−5Fe−30Al), and 68% (15Ni−35Al),

https://doi.org/10.1021/acs.iecr.3c00272
Ind. Eng. Chem. Res. 2023, 62, 11439−11455

which can be caused by an increase of the metal particle size (Figure 10).

The H_2/CO ratio was 1.4 at 900 °C for 15Ni−35Al, which is the highest in the current work (Table 7, entries 1−4). Furthermore, for this catalyst, the H_2/CO ratio was 1.3 at 800 °C. For the 15Ni−5Fe−30Al catalyst, the H_2/CO ratio was 1.3 in the temperature range of 700−900 °C, while also after temperature cycling at 600 °C, it was close to unity (Figure 10d). When the H_2/CO ratio is lower than unity, a reverse water-gas shift reaction (RWGS, $CO_2 + H_2 \rightarrow CO + H_2O$) and/or hydrocarbon oxidation with CO_2 take place.

The initial TOF was also calculated for the mono- and bimetallic catalysts studied in this work (Table 7, entries 1−4). The highest initial TOF was observed for 15Ni−5Fe−30Al, which also exhibited the smallest metal particle size. This result is in accordance with the literature,[61] in which the turnover frequencies in DRM were systematically investigated over four Ni/SiO_2 catalysts exhibiting different metal particle sizes. In another study,[62] the initial TOF decreased with increasing metal particle size.

On comparing the current results with those reported in the literature,[27] it was observed that a bimetallic Ni−Fe/Al_2O_3 catalyst was very active in DRM at 700 °C, yielding 92% methane conversion (Table 7, entry 7). The metal particle size was ca. 10 nm in ref 27, which is the same as that for 15Ni−5Fe−30Al. The highest initial methane conversion was obtained over the Fe−Ni−Al catalyst with an Fe/Ni molar ratio of 0.7 (Table 7, entry 11), while in the current case, the highest methane conversion at 700 °C was obtained with 15Ni−5Fe−30Al with an Fe/Ni molar ratio of 0.26 (Table 7, entry 2).[12] These results, such as conversion levels at both 600 and 700 °C, are quite comparable, with GHSV close to each other.

Comparing the TOF in DRM with the literature data, it can be seen that in the current case, low TOFs were calculated. The main reason for this might be the low specific surface area of the catalyst prepared by the solution combustion method in the current case (Table 7, entries 1−4), wherein, also, relatively large nickel particles (10−26 nm) were present. On the other hand, in the case of Ni/SiO_2[61] and Ni-HMS (HMS denotes hexagonal mesoporous silica),[63] small metal particles with a high metal dispersion promoted catalytic activity. Specific surface areas of Ni/SiO_2 and Ni-HMS were 540 and 728 m^2/g_{cat}, respectively (Table 7, entries 5 and 6).[63,64]

The carbon balance (CB) correlates very well with methane conversion over different catalysts at different temperatures, as demonstrated in Figure 11. The lowest CB was obtained at the highest methane conversion, being independent of acidity.

On comparing the amount of carbon determined by CHNS (Table 6), there is a good correlation with the low carbon amount of 15Ni−15Fe−20Al and 15Ni−25Fe−10Al, and for the most active catalyst 15Ni−5Fe−30Al, a high carbon content was also determined.

The activation energy (E_A) was determined to be 32−51 kJ/mol from methane conversion using the Arrhenius equation (Figure 12). Activation energies reported in the literature for DRM over various Ni-based catalysts are also in the same range, varying from 32 to 56 kJ/mol,[65−68] indicating the absence of mass transfer limitations. This result is in line with a low value of the Weisz−Prater criterion (0.26). It was also reported in ref 65 that when the gas flow rate was increased, the conversion changed only slightly, indicating that external mass transfer limitations for the reactants were not present.

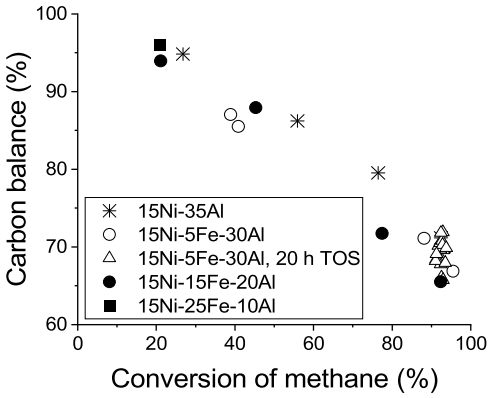

Figure 11. Carbon balance as a function of methane conversion over different catalysts in DRM.

3.7.2. Long-Term Stability. A long-term stability test was conducted over the 15Ni−5Fe−30Al catalyst at the same feed ratio and GHSV for 20 h at 800 °C. Initially, this catalyst displayed CH_4 and CO_2 conversions of 92 and 81%, respectively, as shown in Figure 13, remaining stable for 20 h time-on-stream. The Fe/Ni molar for 15Ni−5Fe−30Al investigated in the current work is 0.26. Furthermore, the yields of H_2 and CO remained the same after 20 h TOS, and the H_2/CO ratio varied in the range of 1.0−1.1 during the experiment. Alterations in this ratio, in general, are caused by the reverse water-gas shift reaction when the excess of hydrogen formed starts to react with CO_2.[59] However, in the current case, with increasing TOS, differences in the yields of CO and H_2 were not significant.

The ratio between the yields of H_2 and CO and TOF for methane consumption generated in the current work at all temperatures and in a long-term experiment are summarized in Figure 14.

It can be seen in Figure 14a that the Y_{H_2}/Y_{CO} ratio increased with increasing reaction rate, and no large differences between different catalysts could be observed. On the other hand, TOF for methane deviated at higher temperatures, as visible for the values for different catalysts at 800 and 900 °C. A higher activity for methane conversion under these conditions was displayed by 15Ni−15Fe−20Al compared to other catalysts (Figure 14b). This might be due to the formation of the Ni−Fe alloy for this catalyst (Figure 1b), and it remained stable during 20 h TOS, together with $NiAl_2O_4$, while no metallic nickel was observed in the spent catalyst (Figure S2).

The catalytic performance of 15Ni−5Fe−30Al was compared with the results obtained with other Ni- and Ni−Fe−Al catalysts (Table 8).

The results showed that CO_2 conversion decreased by only 0.25%/h, indicating rather good stability. Comparison with the literature is, however, not straightforward, because the reaction temperature in the current work was the highest. For a bimetallic 0.3-FeNiAl catalyst, methane conversion decreased only 0.41%/h at 700 °C.[12] It is also noteworthy that highly dispersed monometallic Ni catalysts displayed stable performance in DRM.[63,64] One example is a monometallic Ni/silica catalyst, exhibiting very small nickel particles (Table 7), prepared by the impregnation of citric acid-chelated Ni onto silica, followed by calcination/carbonization.[63] On the other hand, Ni supported on hexagonal mesoporous silica HMS when loading of Ni was achieved by self-assembly exhibited a rather stable performance in DRM at 700 °C even if some sintering occurred for this

https://doi.org/10.1021/acs.iecr.3c00272
Ind. Eng. Chem. Res. 2023, 62, 11439−11455

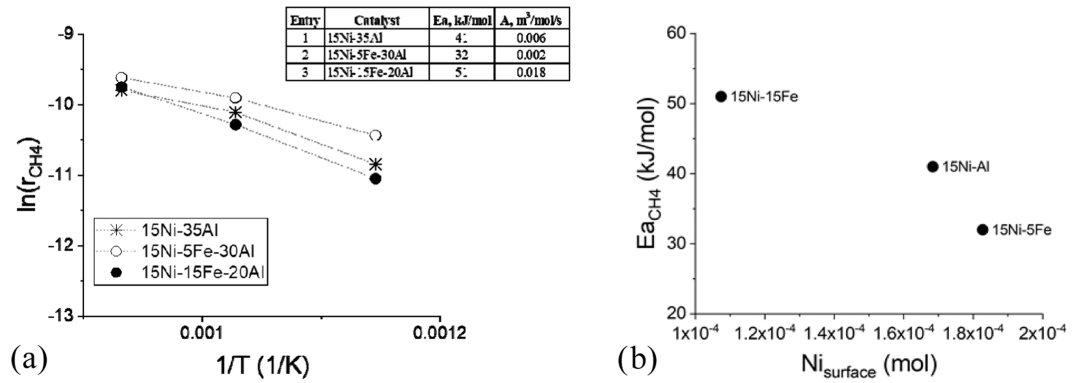

Figure 12. Activation energy: (a) Arrhenius plot and (b) activation energy as a function of the number of moles of exposed Ni on the surface.

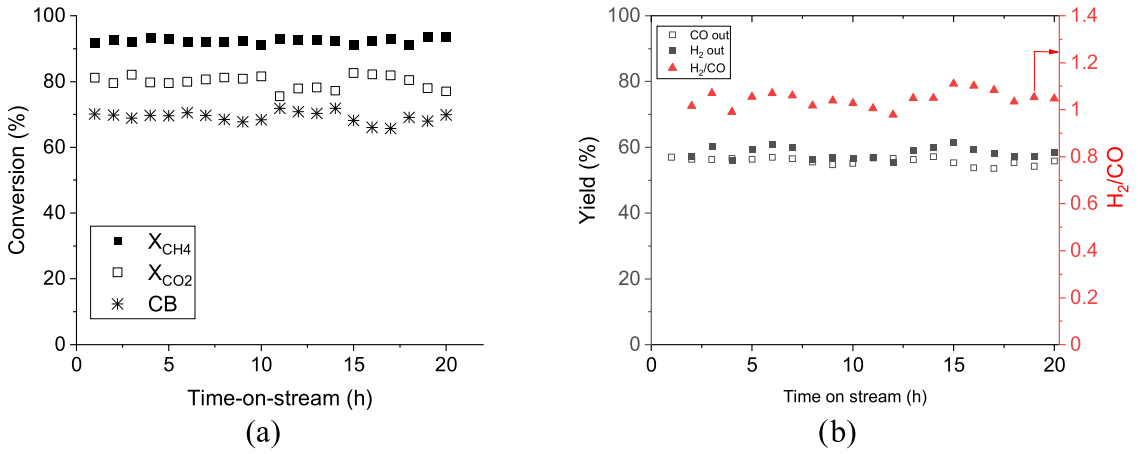

Figure 13. Time-on-stream behavior in a long-term stability test for 15Ni−5Fe−30Al in dry methane reforming at 800 °C using GHSV of 3000 h^{-1}, with $CH_4/CO_2/Ar$ = 1:1:1: (a) conversion of CH_4 and CO_2 and (b) yields of CO and H_2 and the H_2/CO ratio.

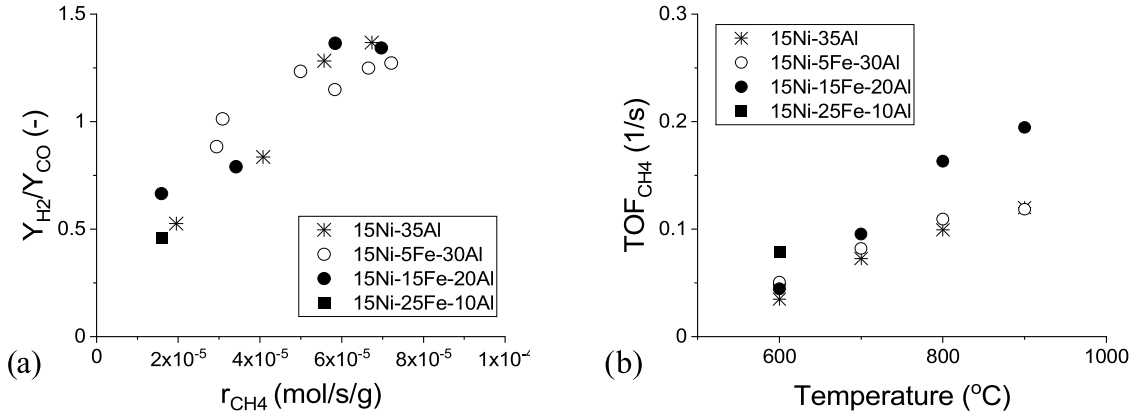

Figure 14. (a) Ratio of H_2/CO yields as a function of the reaction rate of methane. (b) TOF for methane formation as a function of reaction temperature based on the results from Figures 10 and 13.

Table 8. Comparison of Long-Term Activity and Stability of Different Catalysts in DRM

catalyst	conditions	initial X_{CH_4}, %	initial X_{CO_2}, %	initial H_2/CO	Y_{H_2}, %	Y_{CO}, %	TOS, h	[a]deactivation degree, %/h	ref
15Ni−5Fe−30Al	800 °C	92	81	1.0	57	56	20	0.25	this work
0.3-FeNiAl	700 °C	57	63	n.a.	n.a.	n.a.	24	0.41	12
Ni/silica	750 °C	91	84	1.3	n.a.	n.a.	100	0.01	63
Ni-HMS	700 °C	72	83	0.83	n.a.	n.a.	100	0.03	62

[a]Deactivation degree was calculated according to the equation $D_{deact} = \frac{X_{CO_2,r_1} - X_{CO_2,r_2}}{X_{CO_2,r_1}} \times 100\%/t(h)$; X—conversion, %; n.a., not available.

https://doi.org/10.1021/acs.iecr.3c00272
Ind. Eng. Chem. Res. 2023, 62, 11439−11455

catalyst with the nickel particle size increasing from 4.1 to 11.2 nm.[62]

5. CONCLUSIONS

In this work, Ni−Al_2O_3 and bimetallic Ni−Fe−Al_2O_3 catalysts with different Fe/Ni molar ratios were synthesized by the solution combustion synthesis (SCS) and evaluated in the dry reforming of methane. According to XRD, the Ni−Al catalyst contained $NiAl_2O_4$ and metallic Ni phases. For 15Ni−5Fe−30Al, besides metallic Ni, the Ni_3Fe alloy was also found in both fresh and spent catalysts. $NiAl_2O_4$ was reduced to metallic Ni, forming at the same time the Al_3Ni_2 alloy and $Al_{2.667}O_4$. A decrease in catalytic activity for materials with higher Fe loadings is in line with XRD, featuring an inactive $FeAl_2O_4$ spinel for a catalyst with a higher Fe/Ni ratio, as well as with HRTEM, illustrating an increase of the metal particle size. The acidity of catalysts increased with increasing Al concentration in the composition, as could be anticipated. Although TGA, TPO, and CHNS confirmed a high carbon deposition on 15Ni−5Fe−30Al, there was no significant decline in the activity at the lowest temperature, when the reaction temperature was first elevated from 600 to 900 °C and then decreased again. In a 20 h time-on-stream stability test, methane conversion remained constant, while a minor decrease in CO_2 conversion was observed. The H_2/CO ratio was close to unity. The Ni_3Fe phase confirmed by XRD enhanced catalyst stability. The specific surface area (4−16 m^2/g) and pore volume (0.008−0.014 cm^3/g) remained constant, while the median particle size of metals (10−26 nm) decreased during DRM.

■ ASSOCIATED CONTENT

Supporting Information

The Supporting Information is available free of charge at https://pubs.acs.org/doi/10.1021/acs.iecr.3c00272.

Data on long-term stability tests and XRD patterns of the 15Ni−5Fe−30Al catalyst (PDF)

■ AUTHOR INFORMATION

Corresponding Authors

Alua M. Manabayeva − *Kazakh-British Technical University, Almaty 050000, Kazakhstan; Laboratory of Industrial Chemistry and Reaction Engineering, Åbo Akademi University, Turku 20500, Finland; D.V. Sokolsky Institute of Fuel, Catalysis and Electrochemistry, Almaty 050000, Kazakhstan*; Email: manabaeva_2018@mail.ru

Dmitry Yu. Murzin − *Laboratory of Industrial Chemistry and Reaction Engineering, Åbo Akademi University, Turku 20500, Finland*; orcid.org/0000-0003-0788-2643; Email: dmurzin@abo.fi

Authors

Päivi Mäki-Arvela − *Laboratory of Industrial Chemistry and Reaction Engineering, Åbo Akademi University, Turku 20500, Finland*; orcid.org/0000-0002-7055-9358

Zuzana Vajglová − *Laboratory of Industrial Chemistry and Reaction Engineering, Åbo Akademi University, Turku 20500, Finland*

Mark Martinéz-Klimov − *Laboratory of Industrial Chemistry and Reaction Engineering, Åbo Akademi University, Turku 20500, Finland*

Teija Tirri − *Laboratory of Industrial Chemistry and Reaction Engineering, Åbo Akademi University, Turku 20500, Finland*

Tolkyn S. Baizhumanova − *D.V. Sokolsky Institute of Fuel, Catalysis and Electrochemistry, Almaty 050000, Kazakhstan; Al-Farabi Kazakh National University, Almaty 050040, Kazakhstan*

Valentina P. Grigor'eva − *D.V. Sokolsky Institute of Fuel, Catalysis and Electrochemistry, Almaty 050000, Kazakhstan*

Manapkhan Zhumabek − *D.V. Sokolsky Institute of Fuel, Catalysis and Electrochemistry, Almaty 050000, Kazakhstan*

Yermek A. Aubakirov − *Al-Farabi Kazakh National University, Almaty 050040, Kazakhstan*

Irina L. Simakova − *Boreskov Institute of Catalysis, Novosibirsk 630090, Russia*; orcid.org/0000-0002-5138-4847

Svetlana A. Tungatarova − *D.V. Sokolsky Institute of Fuel, Catalysis and Electrochemistry, Almaty 050000, Kazakhstan; Al-Farabi Kazakh National University, Almaty 050040, Kazakhstan*

Complete contact information is available at: https://pubs.acs.org/10.1021/acs.iecr.3c00272

Notes

The authors declare no competing financial interest.

■ ACKNOWLEDGMENTS

This research was funded by the Science Committee of the Ministry of Education and Science of the Republic of Kazakhstan (Grant No. AP14869966). The authors thank the Electron Microscopy Laboratory, Institute of Biomedicine, University of Turku, and Biocenter Finland.

■ REFERENCES

(1) Weiland, P. Biogas production: current state and perspectives. *Appl. Microbiol. Biotechnol.* **2010**, *85*, 849−860.

(2) Angelidaki, I.; Treu, L.; Tsapekos, P.; Luo, G.; Campanaro, S.; Wenzel, H.; Kougias, P. G. Biogas upgrading and utilization: current status and perspectives. *Biotechnol. Adv.* **2018**, *36*, 452−466.

(3) Papadopoulou, C.; Matralis, H.; Verykios, X. Utilization of Biogas as a Renewable Carbon Source: Dry Reforming of Methane. In *Catalysis for Alternative Energy Generation*; Guczi, L.; Erdôhelyi, Eds.; Springer Science+Business Media: New York, 2012; pp 57−127.

(4) Sinha, D.; Banerjee, S.; Mandal, S.; Basu, A.; Banerjee, A.; Balachandran, S.; Mandal, N. C.; Chaudhury, S. Enhanced biogas production from Lantana camara via bioaugmentation of cellulolytic bacteria Debasree. *Bioresour. Technol.* **2021**, *340*, 125652−125661.

(5) Jung, S.; Lee, J.; Moon, D. H.; Kim, K. H.; Kwon, E. E. Upgrading biogas into syngas through dry reforming. *Renewable Sustainable Energy Rev.* **2021**, *143*, 110949−110959.

(6) Dekkar, S. T.; Tezkratt, S.; Sellam, D.; Ikkour, K.; Parkhomenko, K.; Martinez-Martin, A.; Roger, A. C. Dry reforming of methane over Ni−Al_2O_3 and Ni−SiO_2 catalysts: Role of preparation methods. *Catal. Lett.* **2020**, *150*, 2180−2199.

(7) Gonçalves, J. F.; Souza, M. M. V. M. Effect of doping niobia over Ni/Al_2O_3catalysts for methane steam reforming. *Catal. Lett.* **2018**, *148*, 1478−1489.

(8) Alvarez-Galvan, C.; Melian, M.; Ruiz-Matas, L.; Eslava, J. L.; Navarro, R. M.; Ahmadi, M.; Roldan Cuenya, B.; Fierro, J. L. G. Partial oxidation of methane to syngas over nickel-based catalysts: Influence of support type, addition of rhodium, and preparation Method. *Front. Chem.* **2019**, *7*, No. 104.

(9) Shimura, K.; Fujitani, T. Effects of rhodium catalyst support and particle size on dry reforming of methane at moderate temperatures. *Mol. Catal.* **2021**, *509*, 111623−111631.

(10) Zhang, S.; Ying, M.; Yu, J.; Zhan, W.; Wang, L.; Guo, Y.; Guo, Y. $Ni_xAl_1O_{2-\delta}$ mesoporous catalysts for dry reforming of methane: The special role of $NiAl_2O_4$ spinel phase and its reaction mechanism. *Appl. Catal., B* **2021**, *291*, 120074−120091.

(11) Jin, F.; Fu, Y.; Kong, W.; Wang, J.; Cai, F.; Zhang, J.; Xu, J. Dry reforming of methane over trimetallic NiFeCu alloy catalysts. *Chem. Phys. Lett.* **2020**, *750*, 137491−137497.
(12) Li, B.; Luo, Y.; Li, B.; Yuan, X.; Wang, X. Catalytic performance of iron-promoted nickel-based ordered mesoporous alumina FeNiAl catalysts in dry reforming of methane. *Fuel Proc. Technol.* **2019**, *193*, 348−360.
(13) Kim, S. M.; Abdala, P. M.; Margossian, T.; Hosseini, D.; Foppa, L.; Armutlulu, A.; van Beek, W.; Comas-Vives, A.; Copéret, C.; Müller, C. Cooperativity and dynamics increase the performance of NiFe dry reforming catalysts. *J. Am. Chem. Soc.* **2017**, *139*, 1937−1949.
(14) Kwon, Y.; Eichler, J. E.; Mullins, C. B. $NiAl_2O_4$ as a beneficial precursor for Ni/Al_2O_3 catalysts for the dry reforming of methane. *J. CO_2 Util.* **2022**, *63*, 102112−10221.
(15) Abbas, M.; Sikander, U.; Mehran, M. T.; Kim, S. H. Exceptional stability of hydrotalcite derived spinel $Mg(Ni)Al_2O_4$ catalyst for dry reforming of methane. *Catal. Today* **2022**, *403*, 74−85.
(16) Wan, C.; Song, K.; Pan, J.; Huang, M.; Luo, R.; Li, D.; Jiang, L. Ni-Fe/Mg(Al)O alloy catalyst for carbon dioxide reforming of methane: Influence of reduction temperature and Ni-Fe alloying on coking. *Int.J. Hydrogen Energy* **2020**, *45*, 33574−33585.
(17) Al-Mubaddel, F. S.; Kumar, R.; Sofiu, M. L.; Frusteri, F.; Ibrahim, A. A.; Srivastava, V. K.; Kasim, S. O.; Fakeeha, A. H.; Abasaeed, A. E.; Osman, A. I.; Al-Fatesh, A. S. Optimizing acido-basic profile of support in Ni supported La_2O_3-Al_2O_3 catalyst for dry reforming of methane. *Int. J. Hydrogen Energy* **2021**, *46*, 14225−14235.
(18) Manukyan, K. V.; Cross, A.; Roslyakov, S.; Rouvimov, S.; Rogachev, A. S.; Wolf, E. E.; Mukasyan, A. S. Solution combustion synthesis of nano-crystalline metallic materials: Mechanistic studies. *J. Phys. Chem. C* **2013**, *117*, 24417−24427.
(19) Xanthopoulou, G.; Thoda, O.; Boukos, N.; Krishnamurthy, S.; Dey, A.; Roslyakov, S.; Vekinis, G.; Chroneos, A.; Levashov, E. Effects of precursor concentration in solvent and nanomaterials room temperature aging on the growth morphology and surface characteristics of Ni−NiO nanocatalysts produced by dendrites combustion during SCS. *Appl. Sci.* **2019**, *9*, 4925−4945.
(20) Manukyan, K. V. Solution Combustion Synthesis of Catalysts. In *Concise Encyclopedia of Self-Propagating High-Temperature Synthesis*; Elsevier, 2017; pp 347−348.
(21) Novitskaya, E.; Kelly, J. P.; Bhaduri, S.; Graeve, O. A. A review of solution combustion synthesis: an analysis of parameters controlling powder characteristics. *Int. Mater. Rev.* **2021**, *66*, 188−214.
(22) Nandana, B.; Dedhila, D.; Baiju, V.; Sajeevkumar, G. NiAl2O4 Nanocomposite via combustion synthesis for sustainable environmental remediation. *Nanosistemi, Nanomateriali, Nanotehnologii* **2022**, *20*, 459−472.
(23) Sardar, A.; Khader, M. M.; Almarri, M. J.; Abdelmoneim, A. G. Ni-based nano-catalysts for the dry reforming of methane. *Catal. Today* **2019**, *343*, 26−37.
(24) Barroso Quiroga, M. M.; Castro Luna, A. E. Kinetic analysis of rate data for dry reforming of methane. *Ind. Eng. Chem. Res.* **2007**, *46*, 5265−5270.
(25) Murzin, D. Yu. Chemical Reaction. In *Technology*, 2nd ed.; De Gruyter: Berlin, 2022.
(26) Scholten, J. J. F.; Pijpers, A. P.; Hustings, A. M. L. Surface characterization of supported and nonsupported hydrogenation catalysts. *Catal. Rev.* **1985**, *27*, 151−206.
(27) Ferrandon, M. S.; Byron, C.; Celik, G.; Zhang, Y.; Ni, C.; Sloppy, J.; McCormick, R. A.; Booksh, K.; Teplyakov, A. V.; Delferro, M. Grafted nickel-promoter catalysts for dry reforming of methane identified through high-throughput experimentation. *Appl. Catal., A* **2022**, *629*, 118379−118393.
(28) Han, Y. S.; Li, J. B.; Ning, X. S.; Yang, X. Z.; Chi, B. Study on NiO excess in preparing $NiAl_2O_4$. *Mater. Sci. Eng., A* **2004**, *369*, 241−244.
(29) Ray, K.; Deo, G. A potential descriptor for the CO_2 hydrogenation to CH_4 over Al_2O_3 supported Ni and Ni-based alloy catalysts. *Appl.Catal., B* **2017**, *218*, 525−537.
(30) Rahman, M. A.; Ahamed, E.; Faruque, M. R. I.; Islam, M. T. Preparation of $NiAl_2O_4$-based flexible substrates for metamaterials with negative dielectric properties. *Sci. Rep.* **2018**, *8*, No. 14948.
(31) Wang, H.; Kou, X.; Zhang, J.; Li, J. Large scale synthesis and characterization of Ni nanoparticles by solution reaction method. *Bull. Mater. Sci.* **2008**, *31*, 97−100.
(32) Das, S.; Jangam, A.; Du, Y.; Hidajat, K.; Kawi, S. Highly dispersed nickel catalysts via a facile pyrolysis generated protective carbon layer. *Chem. Commun.* **2019**, *55*, 6074−6077.
(33) Han, Y. S.; Li, J. B.; Ning, X. S.; Chi, B. Effect of preparation temperature on the lattice parameter of nickel aluminate spinel. *J. Am. Ceram. Soc.* **2004**, *87*, 1347−1349.
(34) Tayrabekova, S.; Mäki-Arvela, P.; Peurla, M.; Paturi, P.; Eränen, K.; Ergazieva, G. E.; Aho, A.; Murzin, D. Y.; Dossumov, K. Catalytic dehydrogenation of ethanol into acetaldehyde and isobutanol using mono-and multicomponent copper catalysts. *C. R. Chim.* **2018**, *21*, 194−209.
(35) Martínez, R.; Romero, E.; Guimon, C.; Bilbao, R. CO_2 reforming of methane over coprecipitated Ni−Al catalysts modified with lanthanum. *Appl. Catal., A* **2004**, *274*, 139−149.
(36) Marinca, T. F.; Chicinaş, H. F.; Neamţu, B. V.; Isnard, O.; Chicinaş, I. Structural, thermal and magnetic characteristics of Fe_3O_4/Ni_3Fe composite powder obtained by mechano synthesis-annealing route. *J. Alloys Compd.* **2015**, *652*, 313−321.
(37) Theofanidis, S. A.; Galvita, V. V.; Poelman, H.; Marin, G. B. Enhanced carbon-resistant dry reforming Fe-Ni catalyst: Role of Fe. *ACS Catal.* **2015**, *5*, 3028−3039.
(38) Bhattacharyya, A.; Chang, V. W. CO_2 reforming of methane to syngas: deactivation behavior of nickel aluminate spinel catalysts. *Stud. Surf. Sci. Catal.* **1994**, *88*, 207−213.
(39) Sivkov, A. A.; Ivashutenko, A. S.; Rakhmatullin, I. A.; Shanenkova, Yu. L.; Zimmermann, A. I. Study of the phase composition and structure of the nanodispersed Al−O powder produced by a plasmodynamic method. *Nanotechnol. Russia* **2018**, *13*, 76−83.
(40) International Centre for Diffraction Data. Powder Diffraction File (PDF).: Inorganic Phases. Alphabetical indexes. JCPDS. In *International Centre for Diffraction Data*, American Ceramic Society: Florida, U.S.A., 1999, pp 1044
(41) Krasnowski, M.; Gierlotka, S.; Kulik, T. Al_3Ni_2−Al composites with nanocrystalline intermetallic matrix produced by consolidation of milled powders. *Adv. Powder Technol.* **2014**, *25*, 1362−1368.
(42) Qiao, H.; Wei, Z.; Yang, H.; Zhu, L.; Yan, X. Preparation and characterization of NiO nanoparticles by anodic arc plasma method. *J. Nanomater.* **2009**, *2009*, 1−5.
(43) Jastrzębska, I.; Szczerba, J.; Błachowski, A.; Stoch, P. Structure and microstructure evolution of hercynite spinel ($Fe^{2+}Al_2O_4$) after annealing treatment. *Eur. J. Mineral* **2017**, *29*, 63−72.
(44) Paesano, A., Jr.; Matsuda, C. K.; da Cunha, J. B. M.; Vasconcellos, M. A. Z.; Hallouche, B.; Silva, S. L. Synthesis and characterization of Fe-Al_2O_3 composites. *J. Magn. Magn. Mater.* **2003**, *264*, 264−274.
(45) Parsa, M. R.; Soltanieh, M. On the formation of Al_3Ni_2 intermetallic compound by aluminothermic reduction of nickel oxide. *Mater. Charact.* **2011**, *62*, 691−696.
(46) Bian, Z.; Zhong, W.; Yu, Y.; Wang, Z.; Jiang, B.; Kawi, S. Dry reforming of methane on Ni/mesoporous-Al_2O_3 catalysts: Effect of calcination temperature. *Int. J. Hydrogen Energy* **2021**, *46*, 31041−31053.
(47) Song, Z.; Wang, Q.; Guo, C.; Li, S.; Yan, W.; Jiao, W.; Qiu, L.; Yan, X.; Li, R. Improved effect of Fe on the stable $NiFe/Al_2O_3$ catalyst in low-temperature dry reforming of methane. *Ind. Eng. Chem. Res.* **2020**, *59*, 17250−17258.
(48) Kawi, S.; Kathiraser, Y.; Ni, J.; Oemar, U.; Li, Z.; Saw, E. T. Progress in synthesis of highly active and stable nickel-based catalysts for carbon dioxide reforming of methane. *Chem. Sus. Chem.* **2015**, *8*, 3556−3575.
(49) Gao, X.; Lin, W.; Ge, Z.; Ge, H.; Kawi, S. Modification strategies of Ni-based catalysts with metal oxides for dry reforming of methane. *Methane* **2022**, *1*, 139−157.

(50) Zhang, T.; Liu, Z.; Zhu, Y. A.; Liu, Z.; Sui, Z.; Zhu, K.; Zhou, X. Dry reforming of methane on Ni-Fe-MgO catalysts: Influence of Fe on carbon-resistant property and kinetics. *Appl. Catal., B* **2020**, *264*, 118497−118558.
(51) Carrillo, A. J.; Serra, J. M. Exploring the stability of Fe−Ni alloy nanoparticles exsolved from double layered perovskites for dry reforming of methane. *Catalysts* **2021**, *11*, 741−756.
(52) Ray, K.; Sengupta, S.; Deo, G. Reforming and cracking of CH_4 over Al_2O_3 supported Ni, Ni-Fe and Ni-Co catalysts. *Fuel Process. Technol.* **2017**, *156*, 195−203.
(53) Kathiraser, Y.; Thitsartarn, W.; Sutthiumporn, K.; Kawi, S. Inverse $NiAl_2O_4$ on $LaAlO_3$−Al_2O_3: unique catalytic structure for stable CO_2 reforming of methane. *J. Phys. Chem. C* **2013**, *117*, 8120−8130.
(54) Mutz, B.; Belimov, M.; Wang, W.; Sprenger, P.; Serrer, M. A.; Wang, D.; Pfeifer, P.; Kleist, W.; Grunwaldt, J. D. Potential of an alumina supported Ni_3Fe catalyst in the methanation of CO: impact of alloy formation on activity and stability. *ACS Catal.* **2017**, *7*, 6802−6814.
(55) Raso, R.; García, L.; Ruiz, J.; Oliva, M.; Arauzo, J. Aqueous phase hydrogenolysis of glycerol over Ni/Al-Fe catalysts without external hydrogen addition. *Appl. Catal., B* **2021**, *283*, 119598−119611.
(56) Rogers, J. L.; Mangarella, M. C.; D'Amico, A. D.; Gallagher, J. R.; Dutzer, M. R.; Stavitski, E.; Miller, J. T.; Sievers, C. Differences in the nature of active sites for methane dry reforming and methane steam reforming over nickel aluminate catalysts. *ACS Catal.* **2016**, *6*, 5873−5886.
(57) Chareonpanich, M.; Teabpinyok, N.; Kaewtaweesub, S. In *Effect of Nickel Particle Size on Dry Reforming Temperature*, Proceedings of the World Congress on Engineering and Computer Science, October 22−24, 2008.
(58) Tuti, S.; Luisetto, I.; Laverdura, U. P.; Marconi, E. Dry reforming of methane on Ni/nanorod-CeO_2 catalysts prepared by one-pot hydrothermal synthesis: The Effect of Ni content on structure, activity, and stability. *Reactions* **2022**, *3*, 333−351.
(59) Kim, J. H.; Suh, D. J.; Park, T. J.; Kim, K. L. Effect of metal particle size on coking during CO_2 reforming of CH_4 over Ni−alumina aerogel catalysts. *Appl. Catal., A* **2000**, *197*, 191−200.
(60) Han, J. W.; Park, J. S.; Choi, M. S.; Lee, H. Uncoupling the size and support effects of Ni catalysts for dry reforming of methane. *Appl. Catal., B* **2017**, *203*, 625−632.
(61) Park, J. H.; Yeo, S.; Chang, T. S. Effect of supports on the performance of Co-based catalysts in methane dry reforming. *J. CO_2 Util.* **2018**, *26*, 465−475.
(62) Romano, P. N.; de Carvalho Filho, J. F. S.; de Almeida, J. M. A. R.; Sousa-Aguiar, E. F. Screening of mono and bimetallic catalysts for the dry reforming of methane. *Catal. Today* **2022**, *394−396*, 348−356.
(63) Wang, M.; Zhang, Q.; Zhang, T.; Wang, Y.; Wang, J.; Long, K.; Song, Z.; Liu, X.; Ning, P. Facile one-pot synthesis of highly dispersed Ni nanoparticles embedded in HMS for dry reforming of methane. *Chem. Eng. J* **2017**, *313*, 1370−1381.
(64) Das, S.; Jangam, A.; Xi, S.; Borgna, A.; Hidajat, K.; Kawi, S. Highly dispersed Ni/silica by carbonization−calcination of a chelated precursor for coke-free dry reforming of methane. *ACS Appl. Energy Mater.* **2020**, *3*, 7719−7735.
(65) Yusuf, M.; Beg, M.; Ubaidullah, M.; Shaikh, S. F.; Keong, L. K.; Hellgardt, K.; Abdullah, B. Kinetic studies for DRM over high-performance Ni−W/Al2O3−MgO catalyst. *Int. J. Hydrogen Energy* **2022**, *47*, 42150−42159.
(66) Takano, A.; Tagawa, T.; Goto, S. Carbon dioxide reforming of methane on supported nickel catalysts. *J. Chem. Eng. Jpn.* **1994**, *27*, 727−731.
(67) Wang, S.; GQ Max Lu. A comprehensive study on carbon dioxide reforming of methane over Ni/γ-Al_2O_3 catalysts. *Ind. Eng. Chem. Res.* **1999**, *38*, 2615−2625.
(68) Özkara-Aydınoğlu, Ş.; Aksoylu, A. E. A comparative study on the kinetics of carbon dioxide reforming of methane over Pt−Ni/Al_2O_3 catalyst: Effect of Pt/Ni ratio. *Chem. Eng. J.* **2013**, *215−216*, 542−549.

https://doi.org/10.1021/acs.iecr.3c00272
Ind. Eng. Chem. Res. 2023, 62, 11439−11455